Elsevier Editorial System(tm) for Journal of African Earth Sciences
Manuscript Draft

Manuscript Number:

Title: Zircon U-Pb ages and Hf isotope data from the Kukuluma Terrain of the Geita Greenstone Belt, Tanzania Craton: implications for stratigraphy, crustal growth and timing of gold mineralization

Article Type: Research Paper

Keywords: Archean; Tanzania; U-Pb dating; Hf isotopes; Zircon

Corresponding Author: Dr. Ioan Sanislav,

Corresponding Author's Institution: James Cook University

First Author: Kwelwa Shimba

Order of Authors: Kwelwa Shimba; Ioan Sanislav; Paul Dirks; Tom Blenkinsop; Sergio Kolling

Abstract: The Geita Greenstone Belt is a late Archean greenstone belt located in the Tanzania Craton, trends approximately E-W and can be subdivided into three NW-SE trending terrains: the Kukuluma Terrain to the east, the Central Terrain in the middle and the Nyamullilima Terrain in the west. The Kukuluma Terrain, forms a NW-SE trending zone of complexly deformed sediments, intruded by the Kukuluma Intrusive Complex which, contains an early-syntectonic diorite-monzonite suite and a late-syntectonic granodiorite suite. Three gold deposits (Matandani, Kukuluma and Area 3W) are found along the contact between the Kukuluma Intrusive Complex and the sediments. A crystal tuff layer from the Kukuluma deposits returned an age of 2717±12 Ma which can be used to constrain maximum sedimentation age in the area. Two granodiorite dykes from the same deposit and a small granodiorite intrusion found along a road cut yielded zircon ages of 2667±17 Ma, 2661±16 Ma and 2663±11 Ma respectively. One mineralized granodiorite dyke from the Matandani deposit has an age of 2651±14 Ma which can be used to constrain the maximum age of the gold mineralization in the area.
The 2717 Ma crystal tuff has zircon grains with suprachondritic 176Hf/177Hf ratios (0.28108 to 0.28111 at 2717 Ma) and positive (+1.6 to +2.6) εHf values indicating derivation from juvenile mafic crust. Two of the granodiorite samples have suprachondritic 176Hf/177Hf ratios (avg. 0.28106 and 0.28107 at 2663 and 2651 Ma respectively) and nearly chondritic εHf values (avg. -0.5 and -0.3 respectively). The other two granodiorite samples have chondritic 176Hf/177Hf ratios (avg. 0.28104 and 0.28103 at 2667 and 2661 Ma respectively) and slightly negative εHf values (avg. -1.1 and -1.5 respectively). The new zircon age and isotope data suggest that the igneous activity in the Kukuluma Terrain involves a significant juvenile component and occurred within the 2720 to 2620 Ma period which, is the main period of crustal growth in the northern half of the Tanzania Craton.

Suggested Reviewers: Emmanuel Kazimoto
ekazimoto@udsm.ac.tz

Shukrani Manya
shukrani73@udsm.ac.tz

Zubair Jinnah
Zubair.Jinnah@wits.ac.za

Ryan Tucker
tucker@sun.ac.za

Opposed Reviewers:

Dear editor,

Please consider for publication the submitted manuscript. The manuscript is new and original work that was not submitted elsewhere for publication. In this manuscript, we present new field geology data, an updated map of the Geita Greenstone Belt and a first detailed map of the Kukuluma Terrain and new U-Pb ages and Hf isotope data from the Archean Tanzania Craton.

Ioan Sanislav

Graphical Abstract

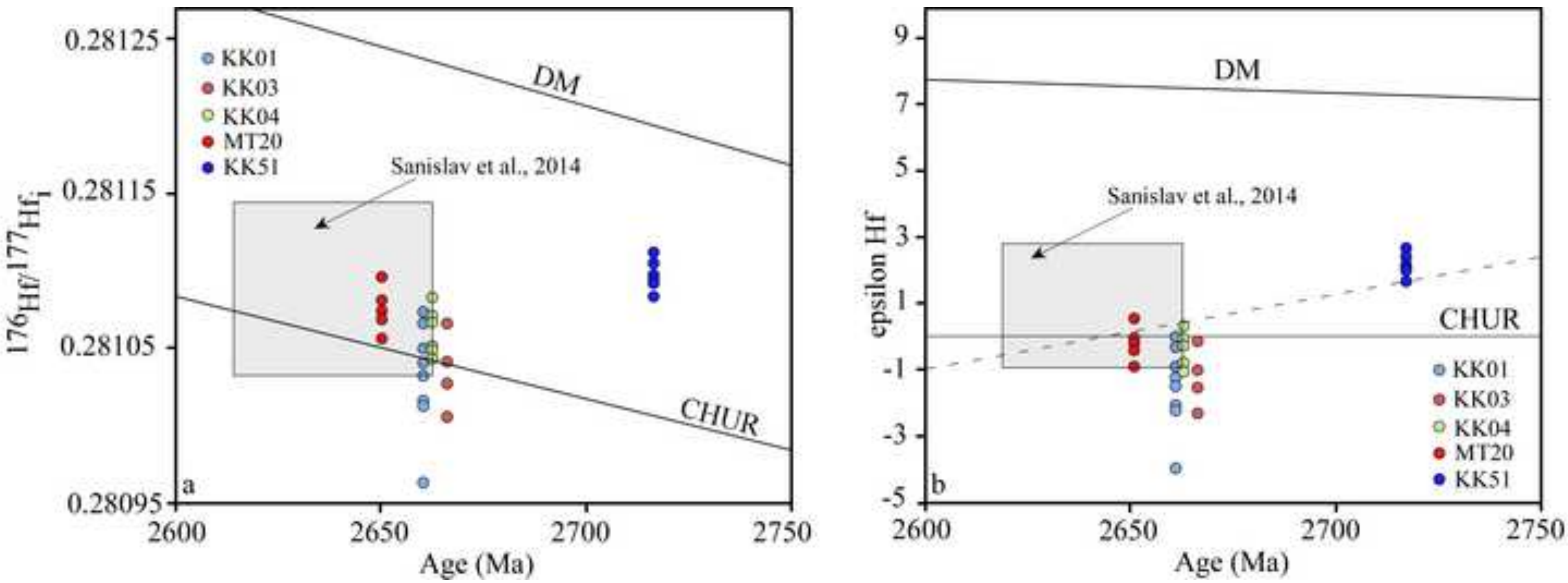

*Highlights

Highlights:

- Kukuluma Terrain forms the eastern part of the Geita Greenstone Belt and hosts three major gold deposits
- The main period of deformation and intrusive activity occurred between 2700 Ma and 2650 Ma
- Crustal growth occurred between 2720 Ma and 2620 Ma from mainly a juvenile source
- The maximum age of gold mineralization is 2650 Ma

Zircon U-Pb ages and Hf isotope data from the Kukuluma Terrain of the Geita Greenstone Belt, Tanzania Craton: implications for stratigraphy, crustal growth and timing of gold mineralization

S. D. Kwelwa[1, 2], I. V. Sanislav[1]*, P. H. G. M. Dirks[1], T. Blenkinsop[3], S. L. Kolling[2]

[1] *Economic Geology Research Centre (EGRU) and Department of Earth and Oceans, James Cook University, Townsville, 4011, QLD, Australia; e-mail: ioan.sanislav@jcu.edu.au; phone: (+61) 07 4781 3293; fax: (+61) 07 4781 5581*

[2] *Geita Gold Mine, Geita, P.O. Box 532, Geita Region, Tanzania*

[3] *School of Earth & Ocean Sciences, Cardiff University, Cardiff CF10 3AT, United Kingdom*

Abstract

The Geita Greenstone Belt is a late Archean greenstone belt located in the Tanzania Craton, trends approximately E-W and can be subdivided into three NW-SE trending terrains: the Kukuluma Terrain to the east, the Central Terrain in the middle and the Nyamullilima Terrain in the west. The Kukuluma Terrain, forms a NW-SE trending zone of complexly deformed sediments, intruded by the Kukuluma Intrusive Complex which, contains an early-syntectonic diorite-monzonite suite and a late-syntectonic granodiorite suite. Three gold deposits (Matandani, Kukuluma and Area 3W) are found along the contact between the Kukuluma Intrusive Complex and the sediments. A crystal tuff layer from the Kukuluma deposits returned an age of 2717±12 Ma which can be used to constrain maximum sedimentation age in the area. Two granodiorite dykes from the same deposit and a small granodiorite intrusion found along a road cut yielded zircon ages of 2667±17 Ma, 2661±16 Ma and 2663±11 Ma respectively. One mineralized granodiorite dyke from the Matandani deposit has an age of 2651±14 Ma which can be used to constrain the maximum age of the gold mineralization in the area.

The 2717 Ma crystal tuff has zircon grains with suprachondritic $^{176}Hf/^{177}Hf$ ratios (0.28108 to 0.28111 at 2717 Ma) and positive (+1.6 to +2.6) εHf values indicating derivation from juvenile mafic crust. Two of the granodiorite samples have suprachondritic $^{176}Hf/^{177}Hf$ ratios (avg. 0.28106 and 0.28107 at 2663 and 2651 Ma respectively) and nearly chondritic εHf values (avg. -0.5 and -0.3 respectively). The other two granodiorite samples have chondritic $^{176}Hf/^{177}Hf$ ratios (avg. 0.28104 and 0.28103 at 2667 and 2661 Ma respectively) and slightly negative εHf values (avg. -1.1 and -1.5 respectively). The new zircon age and isotope data suggest that the igneous activity in the Kukuluma Terrain involves a significant juvenile

component and occurred within the 2720 to 2620 Ma period which, is the main period of crustal growth in the northern half of the Tanzania Craton.

1. Introduction

The architecture of many late Archean cratons such as the Zimbabwe Craton (Kusky, 1998; Jelsma and Dirks, 2002), the Yilgarn Craton (Blewet et al., 2010; Czarnota et al., 2010), the Dharwar Craton (Chadwick et al., 2000; Manikyamba and Kerrich, 2012) or the Superior Province (Percival et al., 2001; Bèdard et al., 2013) is commonly described in terms of a series of terranes assembled along major crustal-scale shear zones. In general, the assembly contains a core of older terrane fragments against which, younger terranes have been juxtaposed in a linear manner, commonly interpreted to indicate terrane accretion analogous to modern day plate tectonic processes (e.g. Zeh et al., 2009; Blewet et al., 2010; Kabete et al., 2012a). Alternative tectonic scenarios include accretion of basaltic plateaus against proto-cratons along dominantly oblique strike-slip shear zones (Bedared et al., 2013) or inversion of intracontinental rift systems sited above mantle plumes (Hayman et al., 2015).

The tectonic architecture of the Tanzania Craton was initially (e.g. Harpum, 1970; Gabert, 1990; Kuehn, 1990) interpreted in terms of a basement unit, the Dodoman Basement Complex, on top of which younger units (the greenstone belts), such as the Nyanzian and the Kavirondian, were thrusted in a process comparable to continental arc tectonics. This interpretation was based mainly on the degree of tectonism described from the above units. The Dodoman Basement Complex comprises mainly high-grade metamorphic rocks including gneiss, migmatite and granulite that formed under mid- to lower crustal conditions, while the Nyanzian and Kavirondian units comprise mainly lower amphibolite to greenschist facies metavolcanics and metasediments. Borg and Shackleton (1997) proposed that the geology of the Nyanzian and the Kavirondian units that occur in the northern half of the

Tanzania Craton is distinct from the gneisses and granulites of the Dodoman Basement Complex that occur to the south and must be treated as a separate tectonic granite-greenstone domain. They subdivided the supra-crustal units in this part of the craton into six individual greenstone belts (Fig. 1) of which the Sukumaland Greenstone Belt is the largest. This interpretation was later confirmed when the first U-Pb zircon dating (Borg and Krogh, 1999) was performed on different units from the Sukumaland Greenstone Belt and it became evident that the gneisses and the migmatites, previously considered basement units, were in part younger that the overlying volcanics and sediments. Subsequent, more extensive U-Pb zircon dating (Manya et al., 2006; Chamberlain and Tosdal, 2007; Mtoro et al., 2009; Kabete et al., 2012b; Sanislav et al., 2014a) revealed that in the northern half of the Tanzania Craton it is common for the 'basement' gneiss, granite intrusions and felsic volcanics incorporated in the greenstone sequence to yield ages that are younger than or similar to the ages obtained from the mafic metavolcanics (dated at ~ 2820 Ma; Manya and Maboko, 2003; Manya and Maboko, 2008; Cook et al., 2016), attributed to the lower Nyanzian units. Following these new findings, the greenstone belts were interpreted to have formed in arc-like settings (e.g Manya and Maboko, 2003; Manya and Maboko, 2008; Mtoro et al., 2009; Mshiu and Maboko, 2012), to represent lateral accretion of exotic terranes (Kabete et al., 2012a) or to be reminiscent of oceanic plateaus (Cook et al., 2016). Thus, different parts of the northern half of the Tanzania Craton record specific geological histories. Manya et al. (2006) proposed that is unlikely that all the greenstone belts in the Tanzania Craton belong to the Nyanzian Supergroup and the geology of each greenstone belt should be treated individually. Moreover, each of the six greenstone belts (Fig. 1) shows a highly-fragmented map pattern. For example, the SGB is made of at least 15 individual greenstone fragments. It is unclear how much of this fragmentation is tectonic in nature, related to the intrusion of plutons or just a consequence of poor outcrop exposure. The lack of detailed studies on most of the greenstone fragments makes it difficult to assess whether they share a common geological history or not. The Geita Greenstone Belt (GGB; Fig. 2; Sanislav et al., 2014a) is one of the largest and the best studied greenstone fragment that occurs within the SGB. It contains stratigraphic elements that can be related to the original description (e.g. Stockley, 1936; Quennel et al., 1956; Harpum, 1970) of the Nyanzian and the Kavirondian successions; a lower mafic unit, overlain by intercalations of shales, ironstones, sandstones, siltstones, mudstones and volcanoclastics which are unconformably overlain by quartzitic conglomerates and grits (Sanislav et al., 2015; Cook et al., 2016). In this contribution, we present U-Pb zircon ages and Hf isotope data from tuffaceous sediments, granodiorite dykes and intrusions from the GGB and discuss their significance in terms of field relationships, timing of gold mineralization, implications for the stratigraphic relationships and for the crustal growth in the Tanzania Craton.

2. Geological framework

The Archaean stratigraphy of the Tanzania craton has been subdivided into three main supergroups, the Dodoman, the Nyanzian and the Kavirondian Supergroups. The Dodoman Supergroup is found mainly in the central part of the Tanzania Craton and is considered to represent the oldest unit in the stratigraphy (e.g. Quennel et al., 1956; Gabert, 1990). It consists of high-grade mafic and felsic granulite with subordinate amounts of lower-grade schists and thin slivers of greenstone belts (Kabete et al., 2012a). The Nyanzian Supergroup was considered to overly the Dodoman Supergroup (e.g. Stockley, 1936; Quennel et al., 1956; Harpum, 1970; Gabert, 1990) but zircon dating (e.g. Borg and Krogh, 1999; Manya et al., 2006; Sanislav et al., 2014a) revealed that gneisses, migmatites and granites that occur with the greenstone belts are commonly younger than the greenstone belt lithologies, and can therefore not be considered basement units. The Nyanzian Supergroup was subdivided into two main units: the Lower Nyanzian and the Upper Nyanzian. The Lower Nyanzian is composed mainly of mafic volcanics metamorphosed to the amphibolite facies (basalt, pillow basalt, minor gabbro) dated at ~2823 Ma (Manya and Maboko, 2003; Manya and Maboko, 2008; Cook et al., 2016) while the Upper Nyanzian is dominated by sedimentary units such as shales, banded ironstone, volcanoclastics and immature sandstone and siltstone, intruded by intermediate to felsic dykes and plutons (Kuehn et al. 1990; Borg, 1992; Borg and Krogh 1999; Sanislav et al., 2017). The Nyanzian Supergroup is metamorphosed to greenschist facies (Quennel et al., 1956; Harpum, 1970) but locally, around granite intrusions records higher metamorphic grades (Borg and Shackleton, 1997).

The Kavirondian Supergroup unconformably overlies the Nyanzian and consists of conglomerate, quartzite, grits, sandstone and siltstone (Stockley, 1936; Harpum, 1970; Borg, 1992), deposited between ~2450 Ma and ~2762 Ma (Gabert, 1990; Sanislav et al., 2015).

The northern half of the Tanzania Craton contains six greenstones belts including: the Nzega, Musoma-Mara, Iramba-Sekenke, Shynianga-Malita, Kilimafedha and the Sukumaland Greenstone Belts (Borg and Shackleton, 1997; Fig. 1). Each of these greenstone belts consists of a series of disconnected greenstone domains/fragments that were grouped together based mainly on their geographic proximity (i.e. the various greenstone portions may not necessarily share a common geological history; Cook et al., 2016). The Sukumaland Greenstone Belt, located south of Lake Victoria is the largest of these greenstone belts and consists of a series of greenstone fragments (Fig. 1) separated by granite plutons, gneissic domains and shear zones. Borg et al. (1990) and Borg (1994) describe the Sukumaland Greenstone Belt as an arcuate-shaped belt intruded by syn- to post-tectonic granitoid of TTG affinity that divide the belt into an inner arc dominated by mafic volcanic rocks and an outer arc dominated by banded ironstone, felsic tuff and volcanoclastic sediments. However, abundant mafic units have been described from the outer arc, although poorly exposed (e.g. Manya and Maboko, 2008; Cook et al., 2016), and sediments and felsic volcanic intercalations are common in the inner arc (e.g. Cloutier et al., 2005; Manya and Maboko, 2008), indicating that the subdivision into an inner and outer arc is an oversimplification of the greenstone stratigraphy in the area (e.g. Cook et al., 2016).

The Geita Greenstone Belt (Fig. 2) forms a 50x25 km large, poorly exposed, greenstone domain in the northern part of the Sukumaland Greenstone Belt. The GGB is bounded to the N, E and W by late syn- to post-tectonic 2660-2620 Ma, high-K granites (Sanislav et al. 2014a) and to the S by TTG gneisses across a large, E-W trending mylonitic shear zone (Fig. 2). The southern part of the GGB contains metabasalts with minor gabbro yielding model ages of ca. 2820 Ma (Manya and Maboko 2008; Cook et al., 2016). The remainder of the greenstone belt is dominated by sediments deposited prior to 2699 Ma (Borg and Krogh, 1999, Sanislav et al., 2015). The sediments are complexly deformed, but in general the sequence starts with shales and continues with ironstone intercalated and overlain by volcanoclastics and sandstone, siltstone and mudstone (see Fig. 3.4). The sequence is intruded by early igneous complexes of diorite and TTG, felsic porphyries and dykes (e.g. Sanislav et al., 2015; 2017).

The ironstones are in general the best exposed units of the GGB and form high hills and ridges across the belt. Based on the geophysics and the outcrop patterns the GGB can be subdivided into three NW-SE trending terrains (Sanislav et al., 2014b): the Nyamulilima Terrain to the W, the Central Terrain in the middle, and the Kukuluma Terrain to the E (Fig. 2). The Nyamulilima Terrain contains three major gold deposits (Ridge 8, Star and Comet and Roberts; Fig. 2) along an approximately NW-SE trend. The Central Terrain contains at least seven major gold deposits with the three largest occurring along a NE-SW mineralized trend including the Geita Hill, the Lone Cone and the Nyankanga deposits (Sanislav et al., 2015, 2017). The Kukuluma Terrain (Fig. 3) contains three major gold deposits (Matandani, Kukuluma and Area 3 West) and two prospects (Area 3 Central and Area 3 South) that are positioned along an approximately E-W trend. The Matandani and the Kukuluma deposits were mined in open pit until 2007 while the Area 3West deposit has not yet been developed, but is extensively mined by artisanal workers. Mining of the Matandani and Kukuluma deposits targeted the oxide zone and stopped when sulfide ore was exposed due to the refractory nature of the arsenopyrite-rich ore. The gold mineralization is hosted along the contact between the Kukuluma Intrusive Complex (KIC) and the complexly deformed metasediments (Kwelwa, 2017).

3. Previous geochronology from the Sukumaland Greenstone Belt and from the Geita Greenstone Belt

The oldest reported zircon ages from the Sukumaland Greenstone Belt (SGB) are from pyroclastic tuffs and range in age from 2821 Ma to 2770 Ma (Borg and Krogh, 1999; Chamberlain and Tosdal, 2007). The oldest zircon age of 2821±30 Ma comes from an altered ash layer of intermediate composition derived from the Tulawaka gold deposit (Chamberlain and Tosdal, 2007), which is located approximately 50 km SW of Geita. From the southern part of the SGB, near Kahama, Borg and Krogh (1999) reported zircon ages of 2808±3 Ma and 2780±Ma from pyroclastic tuffs of rhyolitic composition. Similar zircon ages of 2779±13 Ma and 2770±9 Ma (Chamberlain and Tosdal, 2007) from pyroclastic tuffs of rhyolitic composition were reported from the Nyanzaga area about 100 km E of Geita. From the Nyamullima Terrain in the western part of the GGB a tuff layer interbedded with banded ironstones was dated at 2771±15 Ma (Chamberlain and Tosdal., 2007). The next oldest set of zircon ages was obtained from suites of intrusive rocks of dioritic and tonalitic composition that range in age between 2765 Ma and 2738 Ma (Chamberlain and Tosdal, 2007). The oldest age at 2765±25 Ma comes from a tonalite intrusion near Kahama. The remaining ages come mostly from the Lubando and Imweru areas, W of Geita, where diorite to gabbro-diorite intrusions that were emplaced into the mafic volcanics yield ages ranging between 2758 and

2743 Ma. From the GGB two identical tonalite ages of ~ 2738 Ma are reported by Chamberlain and Tosdal (2007). One of the tonalites intruded the Kiziba Formation in the southern part of the greenstone belt while the other one intruded into the Nyamullilima Terrain. Field observations indicate that the former is strongly deformed; the latter tonalite intrusion could not be identified in the field.

From Bulyanhulu a pyroclastic felsic tuff was dated at 2719±16 Ma and interpreted to indicate a maximum age for volcanic activity in the area while a felsic porphyry dyke dated at 2710±10 Ma was interpreted to indicate the minimum age for the volcanism (Chamberlain and Tosdal, 2007). At Geita Hill a monzodiorite that cuts the ironstones at a low angle and locally follows the stratigraphy was dated at 2699±9 Ma and interpreted to constrain the age of deposition of the ironstones to before 2700 Ma (Borg and Krogh, 1999). From NW of the Nyankanga deposit, chloritic and feldspathic sandstones contain detrital zircons which, returned homogenous ages of 2702±8 Ma, 2699±8 Ma and 2687±16 Ma (Chamberlain and Tosdal, 2007). From the Nyankanga deposit a diorite dyke was dated at 2698±14 Ma and two felsic porphyries and a lamprophyre yielded ages between 2693 and 2686 Ma (Chamberlain and Tosdal, 2007). The felsic porphyries were interpreted to represent a minimum age for volcanic activity in the area, while the lamprophyre dyke, which is mineralised was interpreted to provide a maximum age constrain on the mineralization. The age of mineralisation has been further constrained by (Borg and Krogh, 1999). who obtained a zircon age of 2644±3 Ma for a deformed and mineralized lamprophyre dyke from the Geita Hill deposit. This age has been interpreted to provide a maximum age for the gold mineralization.

From the southern margin of the SGB, Borg and Krogh (1999) report two identical migmatitic gneiss ages of 2680±3 Ma, which, showed that the gneisses that outcrop in the region do not belong to the Dodoman Supergroup and cannot form the basement to the greenstone sequence. From the same area, near Kahama, Chamberlain and Tosdal (2007) reported a consistent granitoid age of 2680±9 Ma.

Two felsic porphyry dykes that intruded near Imweru and Biharamulo, W of the GGB, were dated at 2670±21 Ma and 2667±14 Ma respectively, and were interpreted to provide an estimate for the minimum age of volcanism in the area (Chamberlain and Tosdal, 2007). From S of the GGB, near Samena Hill, and from the granites that crop out north of the GGB, Chamberlain and Tosdal (2007) reported two identical ages of 2666±8 Ma. Sanislav et al., (2014) reported a series of ages ranging from 2661±14 Ma to 2617±11 Ma from the high-K granites that crop out N of the GGB. Similar ages with the high-K granites, were reported from across the SGB, by Chamberlain and Tosdal (2007), including from the Nyankanga deposits (2653±35 Ma), the Kahama area (2656±11 Ma), Kasubuya (2653±10 Ma) and Bukoli (2646±14 Ma). A flow banded rhyolite from near Bulyanhulu dates at 2654±15 Ma and was interpreted to indicate an Upper Nyanzian sedimentation age.

4. New zircon ages from the Kukuluma terrain

4.1. Samples and field relationships

Five samples were dated by LA-ICP-MS at the Advance Analytical Centre at James Cook University. Samples were collected from volcanoclastic sediments, intrusive units belonging to the Kukuluma Intrusive Complex (KIC) and from late-intrusive, feldspar porphyry dykes and intrusions in and around Matandani and Kukuluma pits (Fig. 3). The samples from the KIC contained no zircons or had a very low zircon yield and could not be dated. From five samples including a crystal tuff, three felsic porphyries and a felsic intrusion enough zircon grains were separated to obtain an age.

4.1.1. Sample KK51 – crystal tuff

This sample was collected from the haul road that descends into Kukuluma pit, along the southern wall of the pit (Fig. 3), where a succession of well-bedded sediments intercalated with volcanoclastics is exposed. Sample KK51 was collected from a layer of crystal tuff interbedded with sandstone, siltstone and mudstone (Fig. 4). The sedimentary sequence on this side of the pit is dominated by tight D_3 folds with sub-vertical axial planes and shallowly plunging fold axes (Sanislav et al., 2015; 2017; Kwelwa, 2017). This part of the stratigraphy is interpreted to represent the upper part of the Nyanzian. The crystal tuff layer is approximately 5 to 7 cm thick and contains a high amount of visible feldspar crystals that are up to 2 millimetres in diameter and are embedded in a fine-grained matrix. The feldspar phenocrysts and the matrix have been completely altered to sericite. Small quartz grains (~20%) are visible under the hand lens. No lithic fragments were identified and the layer appears to be compositionally homogenous.

4.2.2. Sample KK01 – granodiorite dyke.

A dyke of granodioritic composition is approximately 1.5 metres (Fig. 4) wide and is well exposed in the W part of Kukuluma pit (Fig. 3). The dyke trends approximately NW-SE and cuts across D_2-D_3 fold interference patterns that are well developed in this part of the pit (Kwelwa, 2017). The dyke also transects the hydrothermal breccia zones that developed along the margins of intrusive diorite-monzonite bodies belonging to the Kukuluma Intrusive Complex (KIC) and intrusions of the KIC itself. The dyke is exposed along the entire height of the W wall of Kukuluma pit and appears to be gently folded by open recumbent folds of D_5 origin. The relationship with D_4 folding is unclear, however, the relative age of emplacement of this dyke occurred at some point between D_3 and D_5. The dyke has been intersected in drill cores where its composition could be better assessed. It is composed of 40% quartz, 35% plagioclase, 20% k-feldspar and ~ 5% mafics (mostly hornblende), and has been classified as granodiorite. There is a visible decrease in grain size at the contact with the brecciated ironstones indicating chilled margins.

4.2.3. Sample KK03 – granodiorite dyke.

A second dyke of granodioritic composition is well exposed along the W wall of Kukuluma pit (Fig. 3). It is about 1 metre thick (Fig. 4) and trends approximately NW-SE. The dyke is porphyritic and highly weathered, but altered feldspar and mafic phenocrysts (hornblende) can still be identified. In fresh drill core its mineralogical composition is near-identical to KK01 above, but it lacks chilled margins. The dyke transects D_3 folds, hydrothermal breccia zones and the KIC, and the dyke has been displaced by D_6 shear zones that run along the margins of the KIC. It's relative time of emplacement is therefore similar to KK01.

4.2.4. Sample KK04 –granodiorite intrusion.

A small granodiorite intrusion (Fig. 3) crops out in a road cutting along the Kukuluma access road (Fig. 5). In this outcrop, well layered sediments intruded by diorite dykes and sills are affected by D_3 and D_4 folds. A penetrative S_3 cleavage is preserved in mudstones and the diorite sills. The granodiorite intrusion is massive and cuts across the layering and the quartz-diorite dykes, but it was affected by a D_6 shear zone which developed along its contact; i.e. the timing of emplacement of this granodiorite body is similar to the timing of the granodiorite dykes described above. The granodiorite is coarse grained, equigranular and is composed of quartz (30-40%), plagioclase (30-40%), k-feldspar (20-30%) and mafics (less than 10%).

4.2.5. Sample MT20 – granodiorite dyke.

A granodiorite dyke cuts across the Matandani deposit along a N-S trend, and the dyke can be traced outside the pit to the Kukuluma access road 300m to the S (Fig. 3). The dyke is up to 3 metres thick (Fig. 6), grey in colour and partly weathered. It contains large plagioclase phenocrysts (~40%), small quartz grains (~30%), altered fine grained k-feldspar

(~25%) and a small amount of altered biotite (~5 %). In fresh samples collected from drill core minor sulfide and iron oxide can also be seen.

In the pit the dyke cuts across the D_2-D_3 interference fold pattern and has not been affected by D_4 and D_5 folding. It also cuts across the D_6 shear zones, the KIC and the tectonic breccias found on in the SW corner of the pit. Along the E margin of the KIC, where the dyke cuts the marginal, D_6 shear zone, the dyke contains slickensided shear fractures attributed to D_7 reactivations along the D_6 shear zone. These fractures did not accommodate visible displacement of the dyke margin, but this sheared part of the dyke does contain low grade mineralization. The relative timing of emplacement of this dyke therefore occurred between D_6 and D_7.

4.3. Results

4.3.1. Geochronology

4.3.1.1. Sample KK51-crystal tuff

Nine of the zircon grains analysed from sample KK-51 yielded analyses with 10% or less discordance (Table 1). The zircon grains are euhedral in shape, luminescent and have concentric zoning without any evidence of relict cores or rim overgrowths (Fig. 7). All zircon grains from this sample show similar cathodoluminescence images suggesting a population derived from the same volcanic source. The $^{207}Pb/^{206}Pb$ ages vary from 2742±18 Ma to 2705±18 Ma with a weighted average age of 2717±12 Ma (Fig. 8a). These ages are similar within error and can be considered to belong to the same age population. The upper concordia age for these zircon grains is 2714±8 Ma (Fig. 8b) which is similar within error to the weighted average $^{207}Pb/^{206}Pb$ age.

4.3.1.2. Sample KK01-granodiorite dyke

This sample contained many zircon grains of different shapes and sizes, and only nine zircon grains returned nearly concordant analyses (≤6% discordance; Table 2). The zircon grains have low luminescence and some grains contain relict cores with a rim overgrowth (Fig. 7). In most cases the relict cores have very low luminescence and are surrounded by a thin line with high luminescence which separates the cores from a rim overgrowth. The relict cores contain high common lead and no reliable age could be calculated while the rim overgrowths were in most situations too thin to be analysed by laser ablation except one grain that contained a rim overgrowth large enough to be analysed (Fig. 7). This rim overgrowth returned a nearly concordant analysis with a $^{207}Pb/^{206}Pb$ age of 2663±19 Ma. The remaining analyses were performed on zircon grains with low luminescence having a faint concentric zoning with no evidence of relict cores or rim overgrowths. Their $^{207}Pb/^{206}Pb$ ages vary between 2684±21 Ma and 2649±18 Ma. The $^{207}Pb/^{206}Pb$ weighted average age for all nine analyses is 2661±16 Ma (Fig. 9a) which is similar within error to the concordia age of 2667±14 Ma (Fig. 9b).

4.3.1.3. Sample KK03-granodiorite dyke

This sample had a low zircon yield, with only ten zircon grains separated. However, six grains returned nearly concordant (≤6% discordance; Table 3) analyses so that age calculations could be performed. The zircon grains vary in shape from short and stubby to elongated grains, and they have low luminescence with a vague concentric zoning (Fig. 7). No relict cores or rim overgrowths were observed. The $^{207}Pb/^{206}Pb$ age of the nearly concordant zircon grains varies between 2687±19 Ma and 2656±20 Ma with an average weighted age of 2667±17 Ma (Fig. 10a). The concordia upper intercept age for this sample is 2658±15 Ma (Fig. 10b).

4.3.1.4. Sample KK04-granodiorite intrusion

Sample KK04 had a very good zircon yield so that a large number of zircon grains could be analysed (Table 4). The zircon grains are euhedral to subhedral and vary in shape from elongated needle-like grains to short and stubby grains. They are low luminescence with a vague concentric zoning (Fig. 7). A few grains contain small relict cores with very low luminescence surrounded by an overgrowth rim. These cores were too small to be analysed. One rim overgrowth analyses returned a $^{207}Pb/^{206}Pb$ age of 2662±20 Ma. The remaining analyses returned $^{207}Pb/^{206}Pb$ ages between 2671±21 Ma and 2648±19 Ma with a weighted average age of 2663±11 Ma (Fig. 11a) and an almost identical upper concordia intercept age of 2662±9 Ma (Fig. 11b).

4.3.1.5. Sample MT20-granodiorite dyke

Seven of the zircon grains analysed from this samples returned nearly concordant ages (≤5% discordance; Table 5). The zircon grains are euhedral with a prismatic shape and medium luminescence. Most zircon grains show a well-developed concentric zoning but several grains have more complex luminescence patterns (Fig. 7). Although, a few zircon grains contained evidence of relict cores they were too small to be dated. The $^{207}Pb/^{206}Pb$ ages of the zircon grains vary between 2660±19 Ma and 2632±20 Ma with a weighted average age of 2651±14 Ma (Fig. 12a) and an almost identical upper concordia age of 2650±8 Ma (Fig. 12b).

4.3.2. Lu-Hf zircon results

Hafnium isotope data is presented in Table 6 and Figure 13. All analysed zircon grains have very low $^{176}Lu/^{177}Hf$ ratios, ranging from 0.00029 to 0.00233, suggesting that following the time of zircon crystallization the $^{176}Hf/^{177}Hf$ ratio of zircon changed little, but the εHf values changed significantly due to the increase of the chondritic $^{176}Hf/^{177}Hf$ ratio over time. The zircon grains from the granodiorite samples have similar Hf isotope compositions with nearly chondritic $^{176}Hf/^{177}Hf_i$ ratios (Fig. 13a) and small εHf variations (Fig. 13b). Sample KK01 shows 4 epsilon units variation, sample KK03 shows 2.2 epsilon units variation, sample KK04 shows only 1 epsilon unit variation and sample MT20 shows 1.4 epsilon units variation between different grains. Overall, the granodiorite samples have a uniform Hf isotope composition with mean $^{176}Hf/^{177}Hf$ ratios of between 0.28107 and 0.28103, and mean εHf values that range from -0.3 to -1.5. The larger spread in Hf isotope composition and the lower εHf values observed in sample KK01could be attributed to the presence of relict cores and possibly to some degree of crustal contamination experienced by this sample.

The zircon grains separated from the crystal tuff sample have suprachondritic $^{176}Hf/^{177}Hf_i$ ratios and positive εHf values. This sample also shows very limited variation in Hf isotope compositions between different grains with a maximum of one epsilon unit difference between analyses.

5. Discussion

5.1. Implications for the deformation history

The Kukuluma Terrain and the Central Terrain share a similar deformation history suggesting that the entire GGB was deformed during the same period. The 2717±12 Ma crystal tuff layer from the Kukuluma pit is interbedded and deformed together with the turbiditic sediments and the ironstones. At the Geita Hill pit in the Central Terrain a trachyandesite dyke dated by Borg and Korgh (1999) at 2699±9 Ma was interpreted by Sanislav et al. (2015) to be one of the monzodiorite dykes that intruded and was folded during D_2 and/or D_3 events. The intrusion of the KIC is most likely synchronous with the intrusion of the diorite dykes in the Central Terrain since both the KIC and the diorite dykes are affected by the D_3 deformation. The granodiorite dykes (samples KK01 and KK03) from the Kukuluma pit and the small granodiorite intrusion (sample KK04) along the Kukuluma access road were emplaced around 2660 Ma. The 2662±6 Ma granodiorite (KK04) intrusion found along the Kukuluma access road cuts across the D_4 fold hinges, the 2661±16 Ma

(KK01) granodiorite dyke from the W wall of the Kukuluma deposit is affected by D_5 sub-horizontal folding while the 2658±15 Ma (KK03) granodiorite dyke from the same side of the deposit is affected by D_6 shearing. These field relationships suggest that the granodiorites were emplaced after D_4, possibly during D_5 and before D_6 deformation. The 2651±14 Ma granodiorite dyke from the Matandani pit has a shear fabric along its margins where it crosscuts the D_6 shear zones without any displacement. Most likely this shear fabric formed very late during D_6 deformation or possibly during D_7 when the D_6 shear zones were reactivated. By comparison, the 2658±15 Ma (sample KK03) granodiorite dyke from the Kukuluma pit is clearly displaced by the D_6 shear zones.

5.2. Implications for the supracrustal stratigraphy

The 2717±12 Ma crystal tuff layer is interbedded with turbiditic sediments and overlies the banded ironstones. The banded ironstones and the turbiditic sediments are in general interpreted to overlie the mafic volcanics of the Kiziba Formation (e.g. Manya and Maboko, 2008; Sanislav et al., 2015; Cook et al., 2015). The whole rock Sm-Nd model ages (Manya and Maboko, 2003; Manya and Maboko, 2008; Cook et al., 2015) indicate that the mafic volcanics were erupted around 2820 Ma, thus forming the oldest identified horizon in the stratigraphy. In the southern part of the GGB where the mafic volcanics are well exposed the contact between the mafic volcanics and the upper part of the stratigraphy is structural (Cook et al., 2015); the metamorphic grade changes from amphibolite facies to lower greenschist facies in less than fifty meters. However, it is unclear whether this structural contact follows an initial unconformity thus, opening the possibility of a sedimentation gap between the eruption of the mafic volcanics and the deposition of the ironstones and the related sediments. It is even less clear whether stratigraphic horizons can be correlated across the GGB or for that purpose across the much larger SGB. For example, the ironstone horizons are the most ubiquitous units across the entire region, have the best surface exposure and a clear geophysical signature but, correlating them across the region is not a straight forward exercise. In the Central Terrain chloritic and feldspathic sandstones that overly the ironstones yielded zircon ages between 2702 and 2687 Ma (Chamberlain and Tosdal, 2007); the field relationships indicate a continuous transition from the ironstones to the sandstones suggesting that the ironstones and the sandstones belong to the same sedimentary cycle. However, in the Nyamullima Terrain (Fig. 2), in the west part of the GGB, a tuff horizon interbedded with the ironstones was dated at 2771±15 Ma (Chamberlain and Tosdal, 2007) indicating ironstone deposition as early as 2770 Ma. Even though, the 2717 Ma crystal tuff layer overlies the ironstones in the Kukuluma Terrain, the ironstone units are interbedded with tuffaceous sediments and show a gradual transition into turbiditic sediments interlayered with volcanoclastics suggesting a continuous sedimentation history. Thus, it is possible, the ironstones, the turbidites and the interlayered volcanoclastics form a continuous unit in the Kukuluma Terrain and possibly the Central Terrain while the ironstones from the Nyamullima Terrain could belong to a separate and maybe older stratigraphic horizon. Further evidence for an older ironstone stratigraphic horizon comes from the Nyanzaga area (Fig. 1), east of the GGB where Chamberlain and Tosdal (2007) reported a 2779±13 Ma age for pyroclastic tuffs overlaying the ironstone units. Pyroclastic flows from near Kahama, the southern part of the SGB, have ages of 2808±6 Ma and 2780±3 Ma (Borg and Krogh, 1999) respectively, also pointing towards an early period of volcanism and sedimentation. Although, the stratigraphic age relationships are poorly constrained, the few available ages point towards the possibility of basin development over a considerable timespan or towards the existence of discrete sedimentation episodes in different basins. Both scenarios require testing in the field and systematic dating of selected stratigraphic horizons.

5.3. Timing of gold mineralization

The gold mineralization is spatially related with the D_6 shear zones which were reactivated during D_7 as normal faults (Kwelwa, 2017). The granodiorite dyke that crosscuts the D_6 shears and the ore zone in the Matandani pit (sample MT20), is mineralised along its margins, where it crosscuts the D_6 shear zones, and can be used to define a maximum age for the timing of gold mineralization in the area. The 2651±14 Ma age of this dyke is similar within error to the 2644±3 Ma age (Borg and Krogh, 1999) of the mineralized lamprophyre dyke from the Geita Hill deposit suggesting that gold mineralization in the Central Terrain and the Kukuluma Terrain may have occurred at about the same time. The gold mineralization in the Matandani pit consists of two sub-parallel mineralisation envelopes occurring on both sides of the KIC. This dyke crosscuts both mineralised envelopes. If the mineralization occurred prior to the emplacement of this dyke, one could expect that the dyke is mineralized across its entire length where it cuts across the ore zone. However, that is not the case. The dyke is mineralised only along thin, discrete shear zones formed along its margins, suggesting that the mineralization postdates the emplacement of this dyke.

5.4. Implications for crustal growth

Four episodes of crustal growth can be recognised in the SGB based on the available zircon ages (Fig. 14). The earliest episode is represented by the extrusion of the ~2820 Ma mafic volcanics (Manya and Maboko, 2003; Manya and Maboko, 2008; Cook et al., 2015) and the associated intermediate volcanics. This is followed between 2780 Ma and 2740 Ma (Fig. 14) by a period dominated by the emplacement of igneous rocks of intermediate composition. A relatively continuous period occurred between 2720 Ma and 2620 Ma, over which magmatism transitions from mainly TTG and diorite in the early stages to the more evolved high-K granites in the later stages. This prolonged period can be subdivided into a

TTG dominated period (2720-2660 Ma) and a high-K granite dominated period (2660-2620 MA). The GGB appears to comprise elements of all the periods of crustal growth with the mafic volcanics being abundant in the southern part of the greenstone belt (Cook et al., 2015), 2770 Ma tuffs occurring in the Nyamullilima Terrain (Chamberlain and Tosdal, 2007) and ~ 2700 Ma diorite and TTG occurring all over the greenstone belt (Sanislav et al., 2015; 2017). The eastern, northern and western side of the greenstone belt are dominated by the 2660 to 2620 ma high-K granites (Sanislav et al., 2014a).

This study presents the first zircon age data for the Kukuluma Terrain. This new dataset indicates that the Kukuluma Terrain was mainly affected by the 2720 to 2620 Ma episode of crustal growth. The 2717±12 Ma crystal tuff was most likely derived from igneous rocks of intermediate or primitive TTG composition as indicated by positive εHf values and suprachondritic $^{176}Hf/^{177}Hf_i$ ratios (Fig. 13). This was followed by the intrusion of the diorite and monzonite phase of the KIC most probably between 2700 and 2680 Ma by comparison with the Nyankanga Intrusive Complex from the Central Terrain (Sanislav et al., 2015; 2017). It is worth noting that the igneous activity in the Kukuluma Terrain follows a similar pattern with the igneous activity in the Central Terrain. That is, an early phase dominated by intrusives of dioritic to monzonitic composition followed by a series of dykes of granodioritic composition (Sanislav et al., 2015; 2017). In the Kukuluma Terrain, the granodiorite phase appears to consistently return ages between 2665 and 2650 Ma marking the transition to the more evolved 2660 to 2620 Ma high-K granites that are wide spread around the margin of the greenstone belt. The nearly chondritic Hf isotope composition of the granodiorites requires a juvenile source for these rocks, most likely of mafic composition which experienced very little interaction with felsic crust. Two samples (KK04 and MT20) have almost identical Hf signatures and basically fall within the chondritic evolution line. The other two samples (KK01 and KK03) have εHf values as low as -4 which, can be explained by the assimilation of some sediment during emplacement. However, their average isotopic signature is still nearly chondritic requiring an important juvenile component in their source. The Hf signature of the granodiorites is almost identical to the Hf signature of the similarly aged high-K granites which also have nearly chondritic affinities indicating crustal growth from a juvenile source, most probably of intermediate composition. The lack of a significant sub-chondritic component in the isotopic signature of zircons precludes any involvement of older felsic crust and the narrow compositional range indicate that little mixing or contamination occurred.

Acknowledgements

This study is part of a PhD study undertaken by the first author at James Cook University. SDK would like to thank James Cook University for waiving the tuition fees and Geita Gold Mine for providing the research funding for this study. Craig Duvel, Hatari Mjinja and the exploration team from Geita Gold Mine are greatly acknowledged for all their support during this project.

Bibliography

Bédard, J.H., Harris, L.B., and Thurston, P.C., 2013. The hunting of the snArc. Precambrian Research, 229, 20-48.

Blewett R.S., Czarnota K., Henson P.A., 2010, Structural-event framework for the eastern Yilgarn craton, Western Australia, and its implications for orogenic gold: Precambrian Research, v. 183, p. 203–229

Borg, G., 1992. New aspects on the lithostratigraphy and evolution of the Siga Hills, an Archaean granite-greenstone terrain in NW-Tanzania. Zeitschrift fur Angewandte Geologie 38 (2), 89-93.

Borg, G., 1994. The Geita gold deposit in NW Tanzania. Geology, ore petrography geochemistry and timing events. Geol. Jb. D 100, 545–595.

Borg, G., Lyatuu, D.R., Rammlmair, D., 1990. Genetic aspects of the Geita and Jubilee reef, Archean BIF-hosted gold deposits, Tanzania. Geol. Rundsch. 79, 355–371.

Borg, G., Shackleton, R.M., 1997. The Tanzania and NE-Zaire Cratons. In: de Wit, M.J., Ashwal, L.D. (Eds.), Greenstone Belts. Oxford University Press, Oxford, pp. 608–619.

Borg. G., and Krogh, T., 1999. Isotopic age data of single zircons from the Archaean Sukumaland Greenstone Belt, Tanzania. Journal of African Earth Sciences 29, 301-312.

Chadwick, B., Vasudev, V.N., Hegde G.V. 2000. The Dharwar Craton, southern India, interpreted as the result of Late Archean oblique convergence. Precambrian Research, 99, pp. 91–11.

Chamberlain, C.M., Tosdal, R.M., 2007. U–Pb geochronology of the Lake Victoria Greenstone Terrane, Tanzania. Mineral Deposit Research Unit The University of British Columbia (Research Program on World-class Gold Deposits and Advanced Exploration Projects Owned and/or Joint Ventured to Barrick Gold, Placer Dome, AngloGold Ashanti, Resolute Mining NL as Main Sponsors.

Cloutier, J., Stevenson, R. K., Bardoux, M., 2005. Nd isotopic, petrologic and geochemical investigation of the Tulawaka East gold deposit, Tanzania Craton. Precambrian Research 139, 147-163.

Cook, Y.A., Sanislav, I.V., Hammerli, J., Blenkinsop, T.G., and Dirks, P.H.G., 2016. A primitive mantle source for the Neoarchean mafic rocks from the Tanzania Craton. Geoscience Frontiers, 7, 911-926.

Czarnota K., Champion D.C., Goscombe B., Blewett R.S., Cassidy K.F., Henson P.A., Groenewald P.B., 2010, Geodynamics of the eastern Yilgarn craton: Precambrian Research, v. 183, no. 2, p. 175–20

Gabert, G., 1990. Lithostratigraphic and tectonic setting of gold mineralization in the Archaean Cratons of Tanzania and Uganda, East Africa. Precambrian Research 46, 59–69.

Harpum, J.R., 1970. Summary of the geology of Tanzania: structure and geotectonics of the Precambrian. Tanzania Geol. Surv. Mem. 1 Part V, 58 pp.

Hayman, P. C., Thébaud, N., Pawley, M. J., Barnes, S. J., Cas, R. A. F., Amelin, Y., Pegg, I., 2015. Evolution of a ~2.7Ga large igneous province: A volcanological, geochemical and geochronological study of the Agnew Greenstone Belt, and new regional correlations for the Kalgoorlie Terrane (Yilgarn Craton, Western Australia). Precambrian Research, 270, 334-368

Jelsma, H.A. and Dirks, P.H.G.M., 2002. Neoarchaean tectonic evolution of the Zimbabwe Craton. In: C.M.R. Fowler, C. Ebinger and C.J. Hawkesworth (Editors), The Early Earth: Physical, Chemical and Biological Development. Geological Society of London Special Publication, 199, 183–211.

Kabete, J.M., Groves, D.I., McNaughton, N.J., Mruma, A.H., 2012a. A new tectonic and temporal framework for the Tanzanian Shield: implications for gold metallogeny and undiscovered endowment. Ore Geology Reviews 48, 88–124.

Kabete, J.M., McNaughton, N.J., Groves, D.I., and Mruma, A.H., 2012b. Reconnaissance SHRIMP U–Pb zircon geochronology of the Tanzania Craton: Evidence for Neoarchean granitoid–greenstone belts in the Central Tanzania Region and the Southern East African Orogen. Precambrian Research 216– 219, 232– 266.

Kuehn, S., Ogola, J., Sango, P., 1990. Regional setting and nature of gold mineralization in Tanzania and southwest Kenya. Precambrian Research 46, 71-82.

Kusky, T.M., 1998. Tectonic setting and terrane accretion of the Archean Zimbabwe Craton. Geology, 26, 163–166.

Kwelwa, S. D., 2017. Geological controls on gold mineralization in the Kukuluma Terrain, Geita Greenstone Belt, NW Tanzania. PhD thesis-James Cook University.

Manikyamba C., Kerrich R. 2012. Eastern Dharwar Craton, India: continental lithosphere growth by accretion of diverse plume and arc terranes. Geoscience Frontiers, 3 , pp. 225–240.

Manya, S., and Maboko, M. A. H., 2003. Dating basaltic volcanism in the Neoarchaean Sukumaland Greenstone Belt of the Tanzania Craton using the Sm–Nd method: implications for the geological evolution of the Tanzania Craton. Precambrian Research 121, 35-45.

Manya, S., Kobayashi, K., Maboko, M.A.H., Nakamura, E., 2006. Ion microprobe zircon U-Pb dating of the late Archean metavolcanics and associated granites of the Musoma-Mara Greenstone Belt, Northeast Tanzania: Implications for the geological evolution of the Tanzanian Craton. Journal of African Earth Sciences 45, 355-366.

Manya, S., Maboko, M.A.H., 2008. Geochemistry of the Neoarchean mafic volcanic rocks of the Geita area, NW Tanzania: implications for stratigraphical relationships in the Sukumaland Greenstone belt. Journal of African Earth Sciences, 52, 152–160.

Mshiu, E.E., and Maboko,M.A.H., 2012. Geochemistry and petrogenesis of the late Archaean high-K granites in the southern Musoma-Mara Greenstone Belt: Their influence in evolution of Archaean Tanzania Craton. Journal of African Earth Sciences 66, 1-12.

Mtoro, M., Maboko, M.A.H., Manya, S., 2009. Geochemistry and geochronology of the bimodal volcanic rocks of the Suguti area in the southern part of the Musoma-Mara Greenstone Belt, Northern Tanzania. Precambrian research 174, 241-257.

Percival, J.A., Stern, R.A., Skulski, T., 2001. Crustal growth through successive arc magmatism: reconnaissance U–Pb SHRIMP data from the northeastern Superior Province, Canada. Precambrian Research 109, 203–238.

Quennell, A.M., McKinley, A.C.M., Aiken, W.G., 1956. Summary of the geology of Tanganyika: introduction and stratigraphy. Tanganyika Geol. Surv. Mem. 1 (Pt. 1) 264 pp.

Sanislav, I. V., Brayshaw, M., Kolling, S. L., Dirks, P. H. G. M., Cook, Y. A., Blenkinsop, T., 2017. The structural history and mineralization controls on the world-class Geita Hill gold deposit, Geita Greenstone Belt, Tanzania. Mineralium Deposita 52, 257-279.

Sanislav, I. V., Wormald, R. J., Dirks, P. H. G. M., Blenkinsop, T. G., Salamba, L., Joseph, D., 2014a. Zircon U-Pb ages and Lu-Hf isotope systematics from late-tectonic granites, Geita greenstone belt: implications for crustal growth of the Tanzania craton. Precambrian research 242, 187-204.

Sanislav, I.V., Dirks, P.H.G.M., Cook, Y.A., Blenkinsop, T.G.,Kolling, S.L., 2014b. A giant gold system, Geita Greenstone Belt, Tanzania. Acta Geologica Sinica 88, 110-111.

Sanislav, I.V., Kolling, S.L., Brayshaw, M., Cook, Y.A., Dirks, P.H.G.M., Blenkinsop, T.G., Mturi, M.I., Ruhega, R., 2015. The geology of the giant Nyankanga gold deposit, Geita Greenstone Belt, Tanzania. Ore Geology Reviews 69, 1-16.

Stockley, G.M., 1936. Geology of the south-eastern regions of the Musoma District. Short Pap. geol. Surv. Tanganyika, 13, 43 pages.

Zeh, A., Gerdes, A. and Barton, J.M., Jr. 2009. Archean accretion and crustal evolution of the Kalahari Craton—the zircon age and Hf isotope record of granitic rocks from Barberton/Swaziland to the Francistown Arc. Journal of Petrology, 50, 933–966.

Figure captions

Figure 1

Geological map of the northern half of the Tanzania Craton (modified from Sanislav et al., 2015). The greenstone belts per Borg and Shackleton (1997): SU – Sukumaland Greenstone Belt; NZ – Nzega Greenstone Belt; SM – Shynianga-Malita Greenstone Belt; IS – Iramba-Sekenke Greenstone Belt; KF – Kilimafedha Greenstone Belt; MM – Musoma-Mara Greenstone Belt. Super-terrane boundaries are as proposed by Kabete et al. (2012a): ELVST – East Lake Victoria, MLEST- Mwanza Lake Eyasi, LNST- Lake Nyanza, MMST – Moyowosi-Manyoni, DBST – Dodoma Basement, MAST – Mbulu-Masai, NBT – Nyakahura-Burigi. Inset map of Africa showing the location of Archean blocks.

Figure 2

Geological map of the Geita Greenstone Belt (modified from Sanislav et al., 2015) showing the approximate location and the age of samples mentioned in text. The ages in bold indicate sedimentation ages.

Figure 3

Geological map of the Kukuluma Terrain showing samples location.

Figure 4

Photographs showing the field relationships for samples KK51 (a), KK01 (b) and KK03 (c). The crystal tuff layer (a) is interlayered with well-bedded immature sandstone, siltstone and mudstone. The dykes are weathered but the massive igneous texture is well preserved. They cut across folded and brecciated ironstones.

Figure 5

Photograph and outcrop sketch showing the field relationships for sample KK04.

Figure 6

Photograph showing the field relationship for sample MT20. This dyke cuts across tight D_2-D_3 folds, the KIC and the D_6 shear zones.

Figure 7

Cathodoluminescence images of zircon grains from sample KK51 (a), KK01 (b), KK03 (c), KK04 (d) and MT20 (e).

Figure 8

Diagrams showing the $^{207}Pb/^{206}Pb$ weighted average age (a) and the concordia age (b) for sample KK51.

Figure 9

Diagrams showing the $^{207}Pb/^{206}Pb$ weighted average age (a) and the concordia age (b) for sample KK01.

Figure 10

Diagrams showing the $^{207}Pb/^{206}Pb$ weighted average age (a) and the concordia age (b) for sample KK03.

Figure 11

Diagrams showing the $^{207}Pb/^{206}Pb$ weighted average age (a) and the concordia age (b) for sample KK04.

Figure 12

Diagrams showing the $^{207}Pb/^{206}Pb$ weighted average age (a) and the concordia age (b) for sample MT20.

Figure 13

Diagrams showing the initial $^{176}Hf/^{177}Hf$ ratios (a) and the εHf values (b) vs. the $^{207}Pb/^{206}Pb$ age of the zircon grains analysed in this study. The shaded areas show the range in Hf isotopic composition for the 2660-2620 Ma high-K granites (Sanislav et al., 2014a).

Figure 14

Probability density diagram showing the distribution of the zircon ages in the Sukumaland Greenstone Belt. Three main periods of crustal growth can be recognised. However, the 2720-2620 Ma period can be separated into a TTG dominated period (2720-2660 Ma) and a high-K granite dominated period (2660-2620 Ma).

Table
Click here to download Table: Tables.docx

Analysis	$^{238}U/^{206}Pb$	Error (1σ)	$^{207}Pb/^{206}Pb$	Error (1σ)	$^{207}Pb/^{235}U$	Error (1σ)	$^{206}Pb/^{238}U$	Error (1σ)	Rho	Age (Ma) $^{207}Pb/^{206}Pb$	Error (1σ)	Age (Ma) $^{206}Pb/^{238}U$	Error (1σ)	Discordance (%)
KK51-01	1.824	0.018	0.186	0.002	14.042	0.149	0.548	0.005	0.94	2705	18	2818	23	-4
KK51-02	2.168	0.022	0.187	0.002	11.876	0.125	0.461	0.005	0.95	2713	18	2445	20	10
KK51-03	1.863	0.019	0.187	0.002	13.818	0.146	0.537	0.005	0.94	2713	18	2770	22	-2
KK51-04	1.886	0.019	0.186	0.002	13.594	0.144	0.530	0.005	0.94	2707	18	2743	22	-1
KK51-05	2.166	0.021	0.187	0.002	11.915	0.125	0.462	0.004	0.93	2718	18	2447	20	10
KK51-06	2.089	0.021	0.187	0.002	12.371	0.130	0.479	0.005	0.94	2720	18	2522	21	7
KK51-07	2.069	0.020	0.190	0.002	12.656	0.133	0.483	0.005	0.92	2742	18	2542	20	7
KK51-08	1.837	0.018	0.187	0.002	14.023	0.145	0.545	0.005	0.94	2714	18	2802	22	-3
KK51-09	2.146	0.021	0.188	0.002	12.063	0.125	0.466	0.004	0.93	2723	18	2466	20	9

Table 1. Table showing the analytical results and the calculated ages for sample KK51.

Analysis	$^{238}U/^{206}Pb$	Error (1σ)	$^{207}Pb/^{206}Pb$	Error (1σ)	$^{207}Pb/^{235}U$	Error (1σ)	$^{206}Pb/^{238}U$	Error (1σ)	Rho	Age (Ma) $^{207}Pb/^{206}Pb$	Error (1σ)	Age (Ma) $^{206}Pb/^{238}U$	Error (1σ)	Discordance (%)
KK01-01	1.960	0.028	0.181	0.004	12.738	0.308	0.510	0.007	0.59	2664	38	2658	31	0
KK01-02	2.102	0.028	0.181	0.002	11.886	0.179	0.476	0.006	0.88	2664	21	2509	28	6
KK01-03	1.977	0.030	0.180	0.003	12.588	0.261	0.506	0.008	0.72	2657	30	2639	32	1
KK01-04	2.112	0.033	0.180	0.006	11.738	0.361	0.473	0.007	0.51	2651	50	2499	32	6
KK01-05	1.972	0.026	0.180	0.002	12.576	0.196	0.507	0.007	0.85	2651	22	2645	29	0
KK01-06	1.969	0.025	0.181	0.002	12.678	0.173	0.508	0.006	0.93	2663	19	2648	27	1
KK01-07	1.935	0.024	0.183	0.002	13.064	0.187	0.517	0.006	0.87	2684	21	2686	27	0
KK01-08	2.073	0.026	0.180	0.002	11.941	0.159	0.482	0.006	0.95	2649	18	2538	26	4
KK01-09	1.976	0.026	0.180	0.003	12.554	0.232	0.506	0.007	0.71	2653	29	2640	29	1

Table 2. Table showing the analytical results and the calculated ages for sample KK01.

Analysis	$^{238}U/^{206}Pb$	Error (1σ)	$^{207}Pb/^{206}Pb$	Error (1σ)	$^{207}Pb/^{235}U$	Error (1σ)	$^{206}Pb/^{238}U$	Error (1σ)	Rho	Age (Ma) $^{207}Pb/^{206}Pb$	Error (1σ)	Age (Ma) $^{206}Pb/^{238}U$	Error (1σ)	Discordance (%)
KK03-01	1.998	0.026	0.180	0.002	12.444	0.178	0.500	0.006	0.90	2656	20	2616	27	2
KK03-02	2.105	0.026	0.182	0.002	11.896	0.159	0.475	0.006	0.93	2668	19	2506	26	6
KK03-03	2.052	0.025	0.181	0.002	12.179	0.164	0.487	0.006	0.92	2665	19	2559	26	4
KK03-04	1.980	0.024	0.181	0.002	12.593	0.166	0.505	0.006	0.93	2661	19	2636	27	1
KK03-05	2.040	0.025	0.184	0.002	12.421	0.163	0.490	0.006	0.92	2687	19	2572	25	4
KK03-06	2.036	0.032	0.181	0.005	12.232	0.320	0.491	0.008	0.60	2658	43	2576	33	3

Table 3. Table showing the analytical results and the calculated ages for sample KK03.

Analysis	$^{238}U/^{206}Pb$	Error (1σ)	$^{207}Pb/^{206}Pb$	Error (1σ)	$^{207}Pb/^{235}U$	Error (1σ)	$^{206}Pb/^{238}U$	Error (1σ)	Rho	Age (Ma) $^{207}Pb/^{206}Pb$	Error (1σ)	Age (Ma) $^{206}Pb/^{238}U$	Error (1σ)	Discordance (%)
KK04-01	1.926	0.023	0.179	0.002	12.843	0.168	0.519	0.006	0.926	2648	19	2696	27	-2
KK04-02	1.928	0.023	0.182	0.002	13.015	0.169	0.519	0.006	0.935	2671	19	2694	27	-1
KK04-03	1.997	0.024	0.180	0.002	12.424	0.163	0.501	0.006	0.927	2653	19	2617	26	1
KK04-04	1.959	0.023	0.181	0.002	12.768	0.165	0.510	0.006	0.920	2666	19	2658	26	0
KK04-05	2.152	0.031	0.180	0.005	11.495	0.295	0.465	0.007	0.553	2651	42	2460	29	7

KK04-06	1.948	0.026	0.182	0.002	12.878	0.193	0.513	0.007	0.880	2672	21	2671	29	0
KK04-07	1.941	0.024	0.182	0.002	12.895	0.170	0.515	0.006	0.922	2667	19	2679	27	0
KK04-08	1.954	0.025	0.181	0.003	12.774	0.197	0.512	0.007	0.835	2664	23	2664	28	0
KK04-09	1.956	0.025	0.181	0.002	12.739	0.193	0.511	0.007	0.850	2661	22	2662	28	0
KK04-10	1.984	0.025	0.181	0.003	12.567	0.194	0.504	0.006	0.801	2661	24	2631	27	1
KK04-11	2.095	0.025	0.181	0.002	11.918	0.158	0.477	0.006	0.899	2662	20	2516	25	5
KK04-12	2.083	0.027	0.181	0.003	11.971	0.224	0.480	0.006	0.683	2661	30	2528	27	5
KK04-13	2.130	0.029	0.181	0.004	11.701	0.272	0.469	0.006	0.589	2659	38	2481	28	7
KK04-14	2.039	0.025	0.182	0.002	12.270	0.160	0.490	0.006	0.927	2667	19	2572	26	4
KK04-15	2.031	0.027	0.181	0.003	12.284	0.197	0.492	0.006	0.823	2663	24	2581	28	3
KK04-16	2.211	0.032	0.182	0.003	11.319	0.213	0.452	0.007	0.774	2668	28	2405	29	10

Table 4. Table showing the analytical results and the calculated ages for sample KK04.

Analysis	$^{238}U/^{206}Pb$	Error (1σ)	$^{207}Pb/^{206}Pb$	Error (1σ)	$^{207}Pb/^{235}U$	Error (1σ)	$^{206}Pb/^{238}U$	Error (1σ)	Rho	Age (Ma) $^{207}Pb/^{206}Pb$	Error (1σ)	Age (Ma) $^{206}Pb/^{238}U$	Error (1σ)	Discordance (%)
MT20-01	1.845	0.018	0.180	0.002	13.454	0.158	0.542	0.005	0.84	2654	20	2791	22	-5
MT20-02	1.884	0.019	0.180	0.002	13.161	0.146	0.531	0.005	0.90	2651	19	2745	22	-4
MT20-03	2.011	0.021	0.178	0.002	12.195	0.144	0.497	0.005	0.86	2632	20	2602	22	1
MT20-04	1.981	0.019	0.181	0.002	12.575	0.130	0.505	0.005	0.92	2660	18	2634	21	1
MT20-05	1.893	0.018	0.181	0.002	13.159	0.133	0.528	0.005	0.93	2659	18	2735	21	-3
MT20-06	1.855	0.018	0.180	0.002	13.364	0.136	0.539	0.005	0.93	2651	18	2780	22	-5
MT20-07	2.004	0.019	0.179	0.002	12.323	0.144	0.499	0.005	0.83	2645	20	2610	21	1

Table 5. Table showing the analytical results and the calculated ages for sample MT20.

Analyses	$^{176}Lu/^{177}Hf$	1 σ	$^{176}Hf/^{177}Hf$	1 σ	$^{176}Hf/^{177}Hf_i$	2 σ	εHf_0	εHf_i	2 σ
				KK01					
KK01-01	0.000629	0.000031	0.280993	0.000022	0.280961	0.000022	-63.4	-4.0	0.8
KK01-02	0.000850	0.000035	0.281082	0.000010	0.281039	0.000010	-60.2	-1.2	0.3
KK01-03	0.001280	0.000015	0.281080	0.000017	0.281015	0.000017	-60.3	-2.1	0.6
KK01-04	0.000932	0.000013	0.281096	0.000007	0.281048	0.000007	-59.7	-0.9	0.3
KK01-05	0.000294	0.000003	0.281080	0.000007	0.281065	0.000007	-60.3	-0.3	0.2
KK01-06	0.000363	0.000003	0.281091	0.000007	0.281073	0.000007	-59.9	0.0	0.2
KK01-07	0.000687	0.000008	0.281066	0.000010	0.281031	0.000010	-60.8	-1.5	0.4
KK01-08	0.001858	0.000076	0.281105	0.000012	0.281011	0.000012	-59.4	-2.2	0.4
				KK03					
KK03-1	0.000527	0.000002	0.281091	0.000008	0.281064	0.000008	-59.9	-0.2	0.3
KK03-2	0.000373	0.000004	0.281083	0.000009	0.281064	0.000009	-60.2	-0.2	0.3
KK03-3	0.000469	0.000007	0.281064	0.000010	0.281040	0.000010	-60.9	-1.1	0.3
KK03-4	0.001171	0.000025	0.281085	0.000017	0.281025	0.000017	-60.1	-1.6	0.6
KK03-5	0.001248	0.000029	0.281067	0.000041	0.281003	0.000041	-60.7	-2.4	1.5
				KK04					
KK04-1	0.000397	0.000013	0.281062	0.000007	0.281042	0.000007	-60.9	-1.1	0.3
KK04-2	0.001456	0.000028	0.281125	0.000011	0.281051	0.000011	-58.7	-0.8	0.4
KK04-3	0.001469	0.000042	0.281124	0.000012	0.281049	0.000012	-58.7	-0.8	0.4
KK04-4	0.000824	0.000015	0.281107	0.000010	0.281065	0.000010	-59.3	-0.3	0.4
KK04-5	0.000581	0.000018	0.281079	0.000008	0.281049	0.000008	-60.3	-0.8	0.3
KK04-6	0.000543	0.000004	0.281070	0.000008	0.281043	0.000008	-60.6	-1.0	0.3
KK04-7	0.000871	0.000011	0.281126	0.000008	0.281081	0.000008	-58.7	0.3	0.3
KK04-8	0.000850	0.000006	0.281113	0.000009	0.281070	0.000009	-59.1	-0.1	0.3
KK04-9	0.000850	0.000006	0.281113	0.000009	0.281070	0.000009	-59.1	-0.1	0.3
				MT20					
MT20-1	0.000468	0.000018	0.281093	0.000009	0.281069	0.000009	-59.8	-0.4	0.3
MT20-2	0.002329	0.000062	0.281197	0.000016	0.281079	0.000016	-56.2	0.0	0.6
MT20-3	0.001047	0.000020	0.281148	0.000011	0.281095	0.000011	-57.9	0.5	0.4
MT20-4	0.001183	0.000021	0.281132	0.000013	0.281072	0.000013	-58.5	-0.3	0.5
MT20-5	0.000452	0.000002	0.281095	0.000007	0.281072	0.000007	-59.8	-0.3	0.2
MT20-6	0.000857	0.000010	0.281098	0.000009	0.281055	0.000009	-59.7	-0.9	0.3
MT20-7	0.000644	0.000006	0.281101	0.000009	0.281068	0.000009	-59.5	-0.4	0.3
				KK51					
KK51-1	0.000914	0.000012	0.281130	0.000009	0.281083	0.000009	-58.5	1.6	0.3
KK51-2	0.000970	0.000005	0.281161	0.000008	0.281111	0.000008	-57.4	2.6	0.3
KK51-3	0.001115	0.000009	0.281153	0.000009	0.281095	0.000009	-57.7	2.1	0.3
KK51-4	0.001076	0.000013	0.281147	0.000010	0.281091	0.000010	-57.9	1.9	0.4
KK51-5	0.000448	0.000009	0.281126	0.000008	0.281103	0.000008	-58.7	2.4	0.3
KK51-6	0.000805	0.000005	0.281136	0.000010	0.281094	0.000010	-58.3	2.0	0.4
KK51-7	0.000840	0.000007	0.281140	0.000007	0.281096	0.000007	-58.2	2.1	0.2

Table 6. Table showing the Hf isotope data for the zircon grains analysed in this study.

Figures

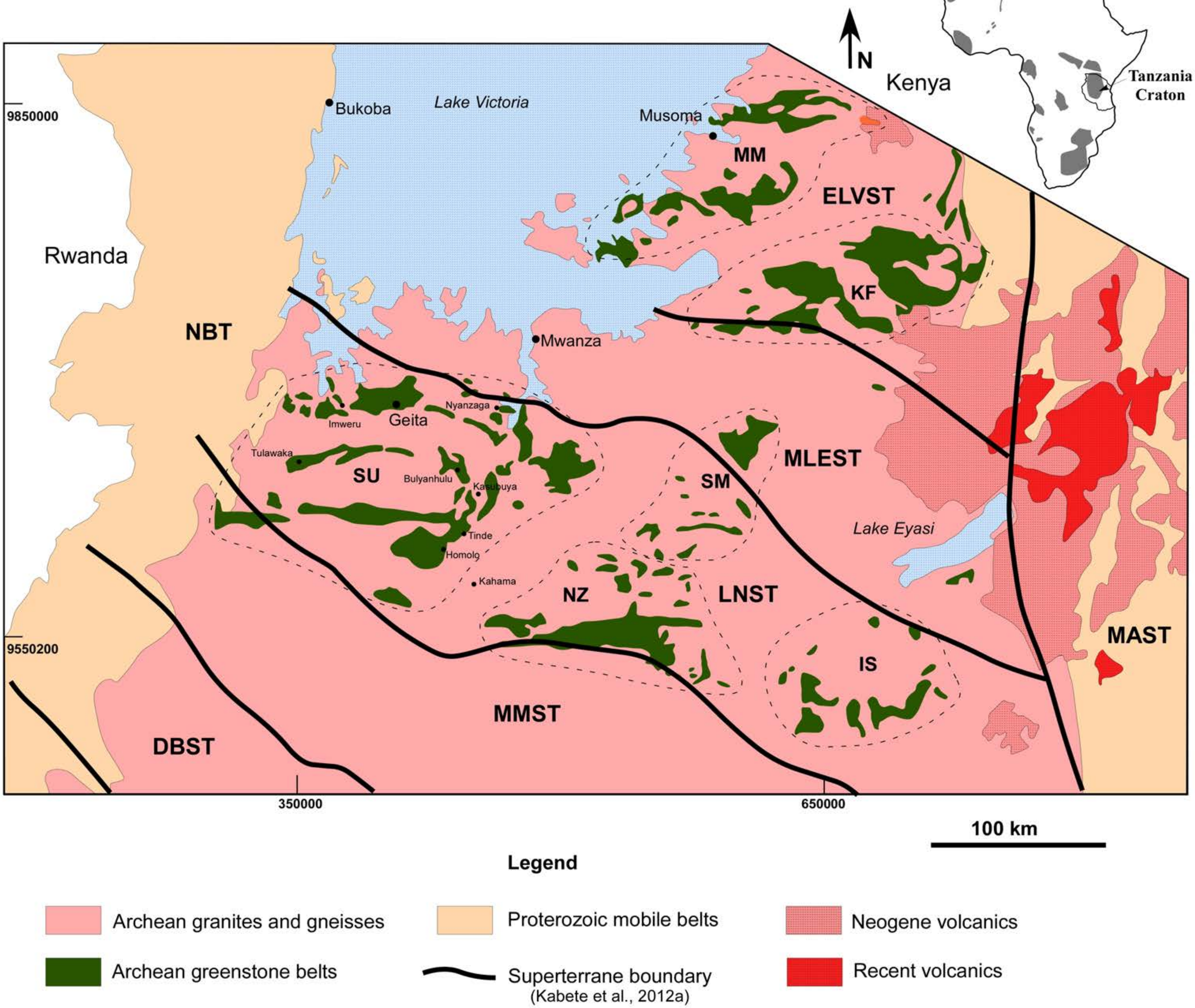

Figure 1

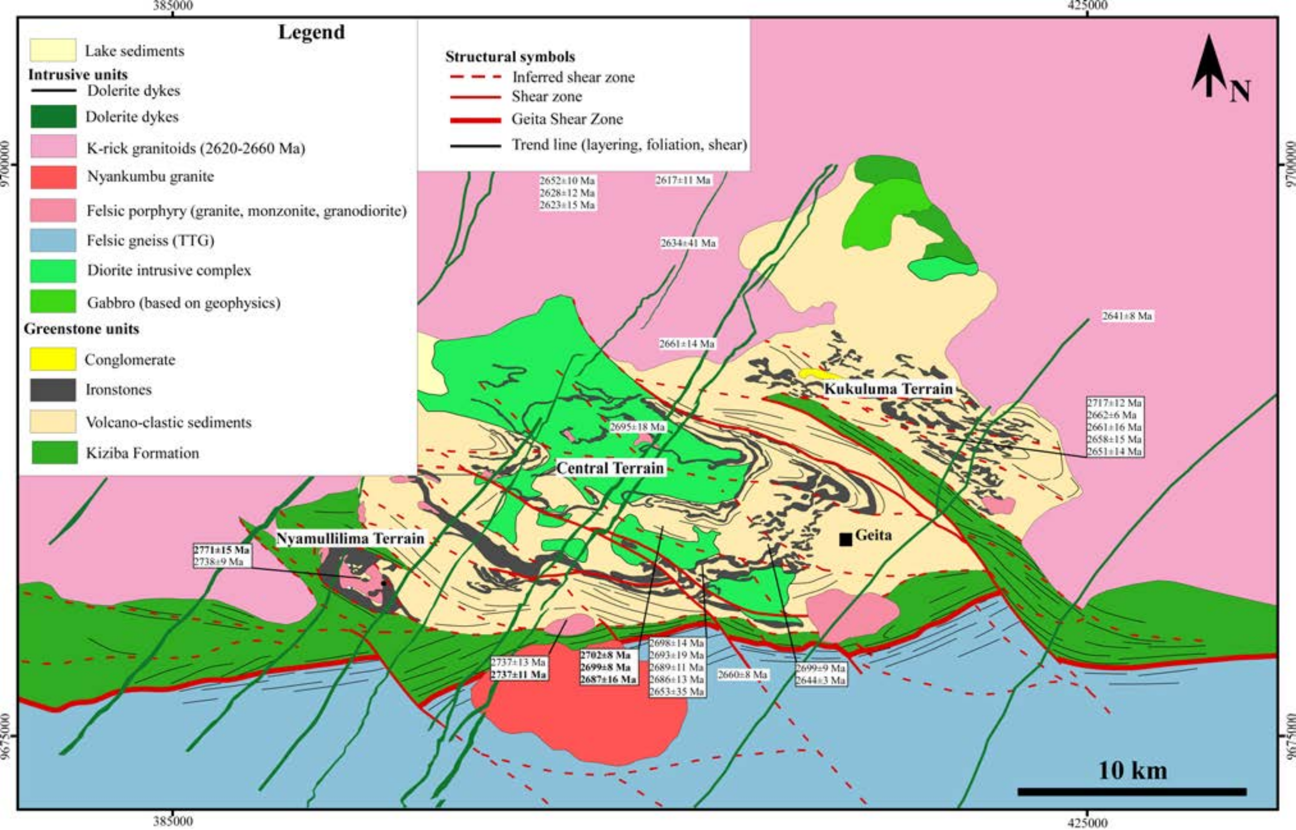

385000
425000
9700000
9675000
Legend
Lake sediments
Intrusive units
Dolerite dykes
Dolerite dykes
K-rick granitoids (2620-2660 Ma)
Nyankumbu granite
Felsic porphyry (granite, monzonite, granodiorite)
Felsic gneiss (TTG)
Diorite intrusive complex
Gabbro (based on geophysics)
Greenstone units
Conglomerate
Ironstones
Volcano-clastic sediments
Kiziba Formation
Structural symbols
Inferred shear zone
Shear zone
Geita Shear Zone
Trend line (layering, foliation, shear)
N
2652±10 Ma
2628±12 Ma
2623±15 Ma
2617±11 Ma
2634±41 Ma
2641±8 Ma
2661±14 Ma
Kukuluma Terrain
2717±12 Ma
2662±6 Ma
2661±16 Ma
2658±15 Ma
2651±14 Ma
2695±18 Ma
Central Terrain
Geita
Nyamullilima Terrain
2771±15 Ma
2738±9 Ma
2737±13 Ma
2737±11 Ma
2702±8 Ma
2699±8 Ma
2687±16 Ma
2698±14 Ma
2693±19 Ma
2689±11 Ma
2686±13 Ma
2653±35 Ma
2660±8 Ma
2699±9 Ma
2644±3 Ma
10 km

Figure 2

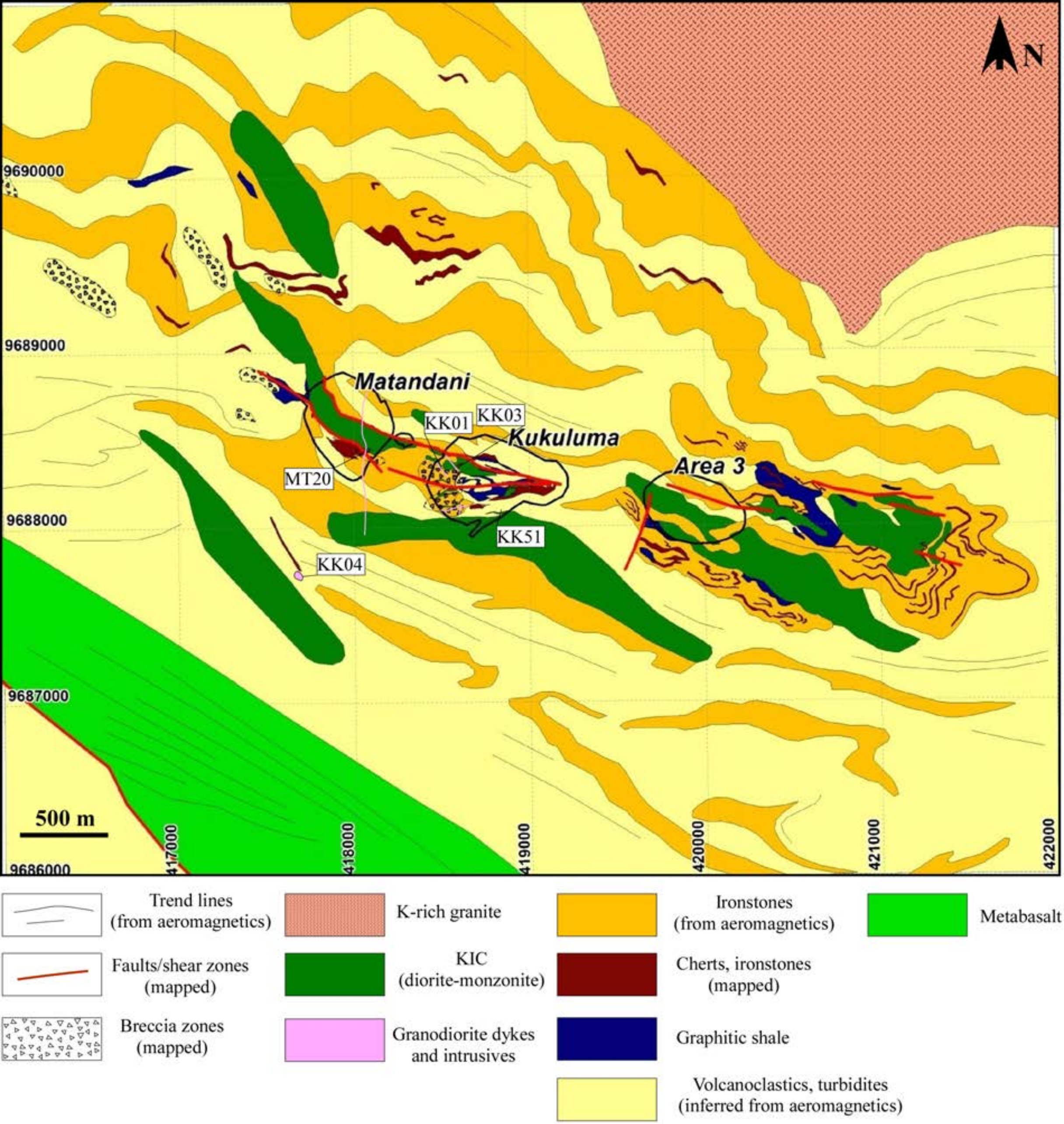
N
9690000
9689000
9688000
9687000
9686000
417000
418000
419000
420000
421000
422000
500 m
Matandani
Kukuluma
Area 3
KK01
KK03
MT20
KK51
KK04
Trend lines (from aeromagnetics)
Faults/shear zones (mapped)
Breccia zones (mapped)
K-rich granite
KIC (diorite-monzonite)
Granodiorite dykes and intrusives
Ironstones (from aeromagnetics)
Cherts, ironstones (mapped)
Graphitic shale
Volcanoclastics, turbidites (inferred from aeromagnetics)
Metabasalt

Figure 3

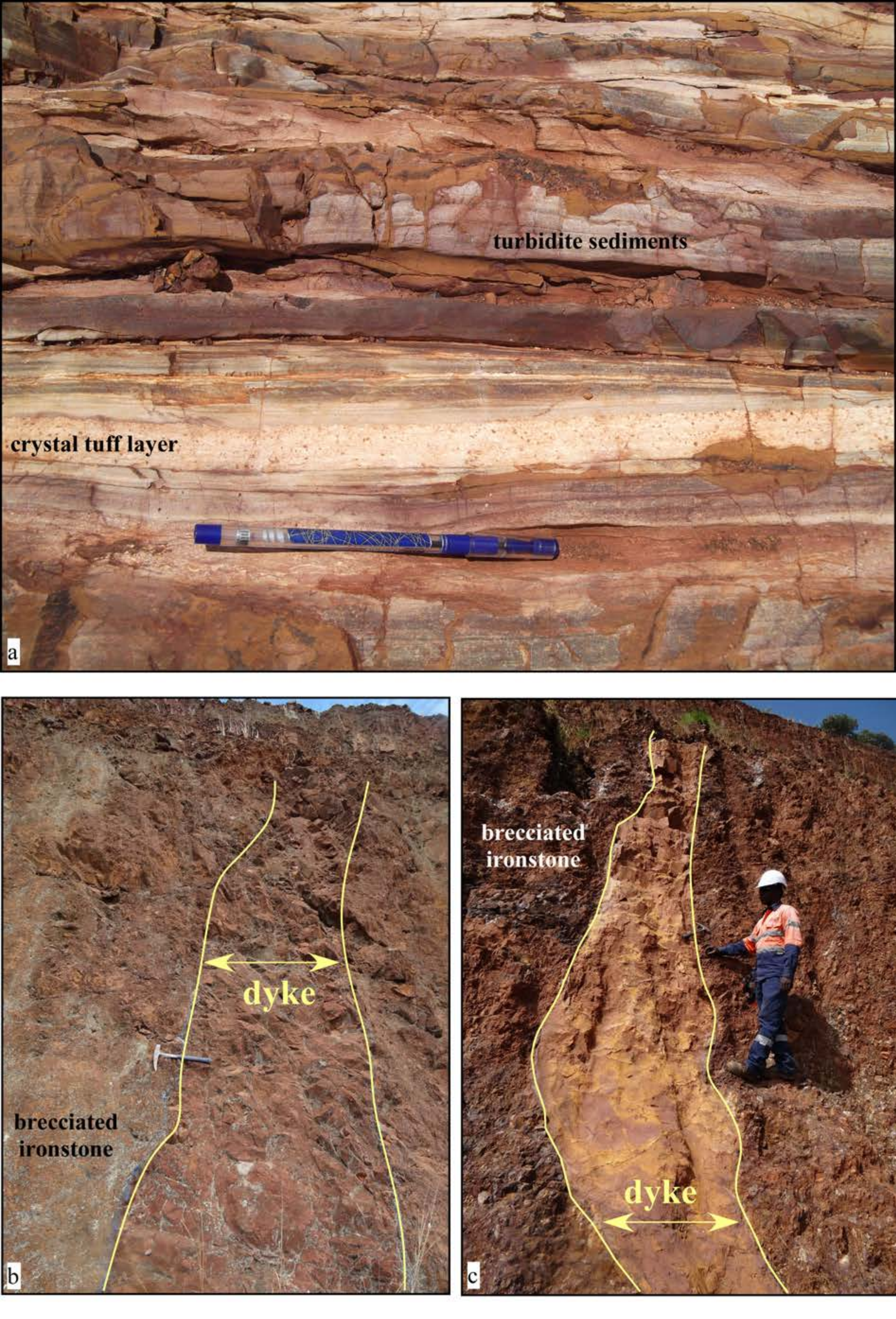
turbidite sediments
crystal tuff layer
a
dyke
brecciated
ironstone
b
brecciated
ironstone
dyke
c

Figure 4

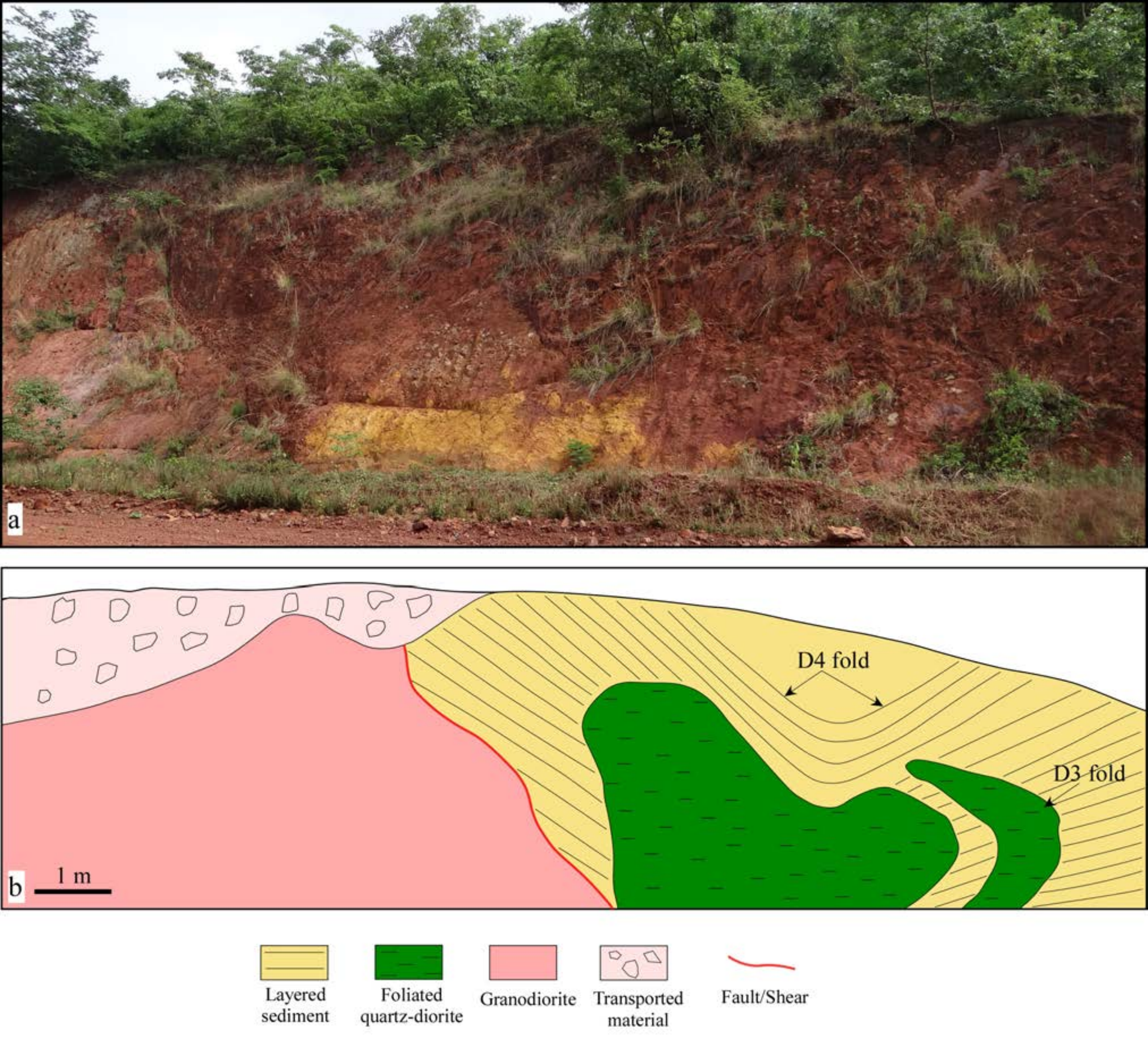
a
D4 fold
D3 fold
b
1 m
Layered sediment
Foliated quartz-diorite
Granodiorite
Transported material
Fault/Shear

Figure 5

Figure 6

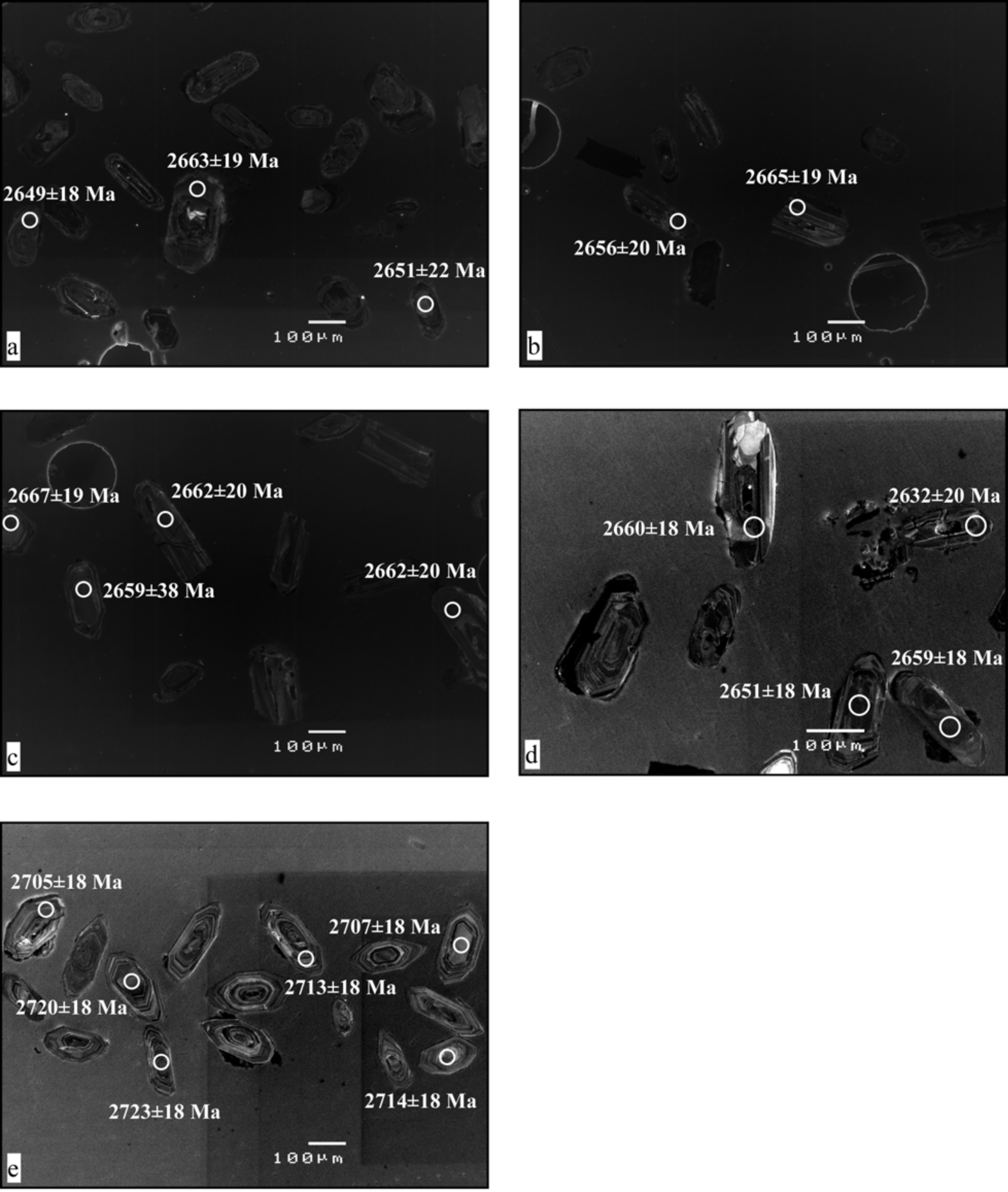
2663±19 Ma
2649±18 Ma
2651±22 Ma
100μm
a
2665±19 Ma
2656±20 Ma
100μm
b
2667±19 Ma
2662±20 Ma
2659±38 Ma
2662±20 Ma
100μm
c
2660±18 Ma
2632±20 Ma
2659±18 Ma
2651±18 Ma
100μm
d
2705±18 Ma
2707±18 Ma
2713±18 Ma
2720±18 Ma
2723±18 Ma
2714±18 Ma
100μm
e

Figure 7

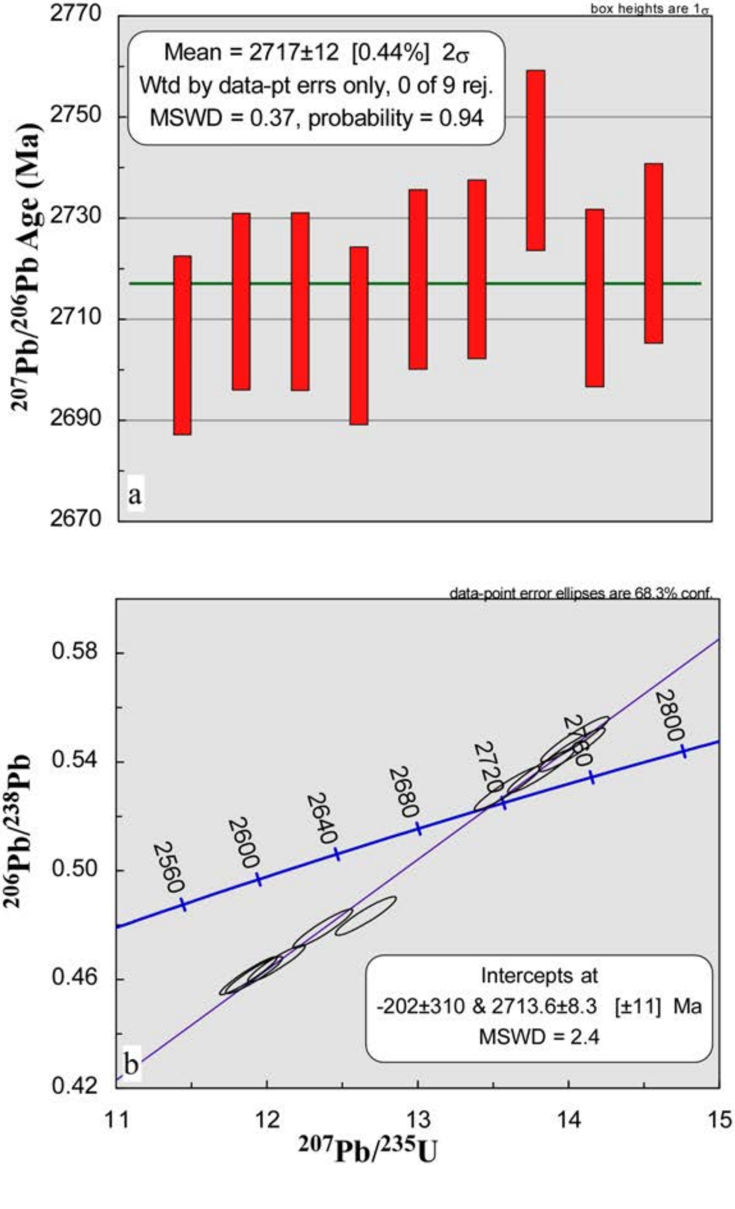

box heights are 1σ
Mean = 2717±12 [0.44%] 2σ
Wtd by data-pt errs only, 0 of 9 rej.
MSWD = 0.37, probability = 0.94
2770
2750
2730
2710
2690
2670
207Pb/206Pb Age (Ma)
a
data-point error ellipses are 68.3% conf.
0.58
0.54
0.50
0.46
0.42
206Pb/238Pb
2560
2600
2640
2680
2720
2760
2800
Intercepts at
-202±310 & 2713.6±8.3 [±11] Ma
MSWD = 2.4
b
11
12
13
14
15
207Pb/235U

Figure 8

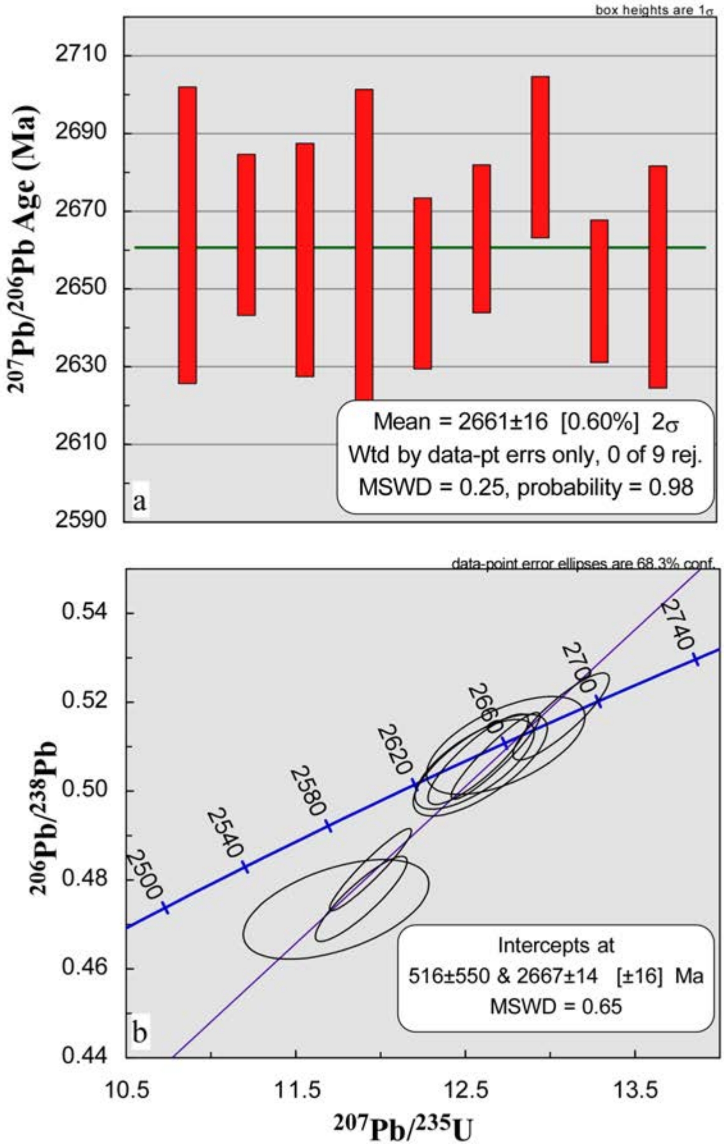
box heights are 1σ
2710
2690
2670
2650
2630
2610
2590
207Pb/206Pb Age (Ma)
Mean = 2661±16 [0.60%] 2σ
Wtd by data-pt errs only, 0 of 9 rej.
MSWD = 0.25, probability = 0.98
a
data-point error ellipses are 68.3% conf.
0.54
0.52
0.50
0.48
0.46
0.44
206Pb/238Pb
2500
2540
2580
2620
2660
2700
2740
Intercepts at
516±550 & 2667±14 [±16] Ma
MSWD = 0.65
b
10.5
11.5
12.5
13.5
207Pb/235U

Figure 9

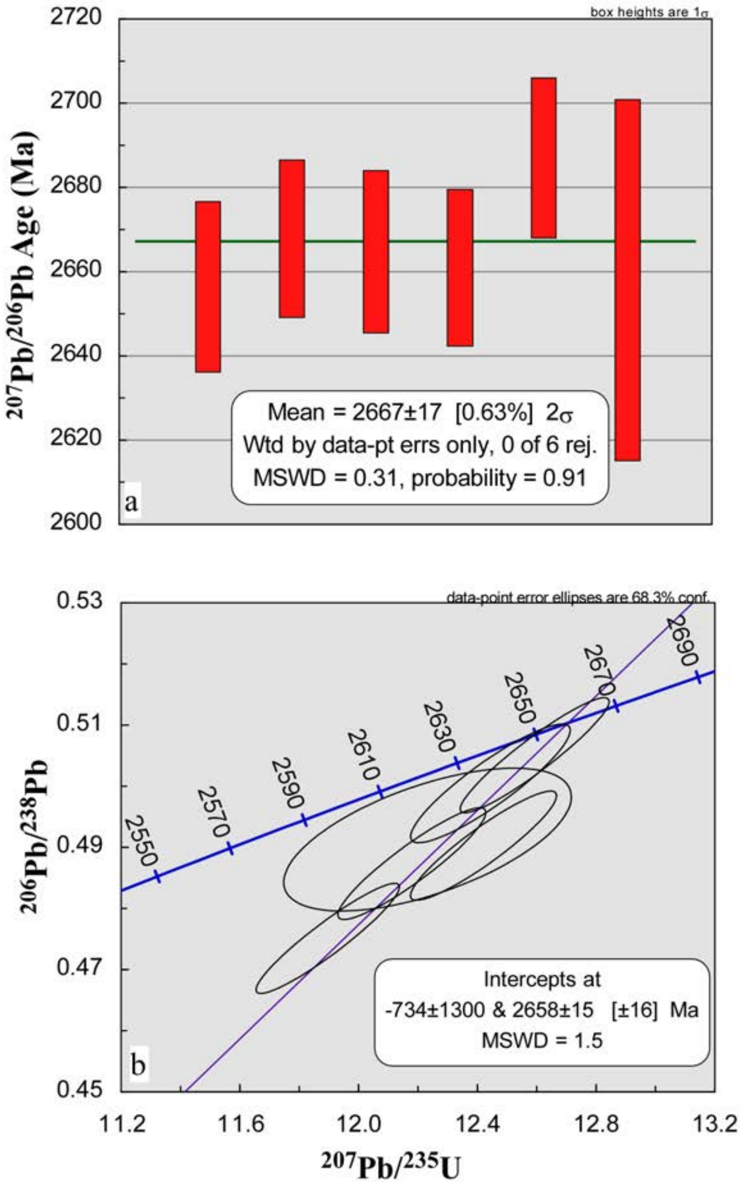
box heights are 1σ
Mean = 2667±17 [0.63%] 2σ
Wtd by data-pt errs only, 0 of 6 rej.
MSWD = 0.31, probability = 0.91
a
207Pb/206Pb Age (Ma)
data-point error ellipses are 68.3% conf.
Intercepts at
-734±1300 & 2658±15 [±16] Ma
MSWD = 1.5
b
206Pb/238Pb
207Pb/235U

Figure 10

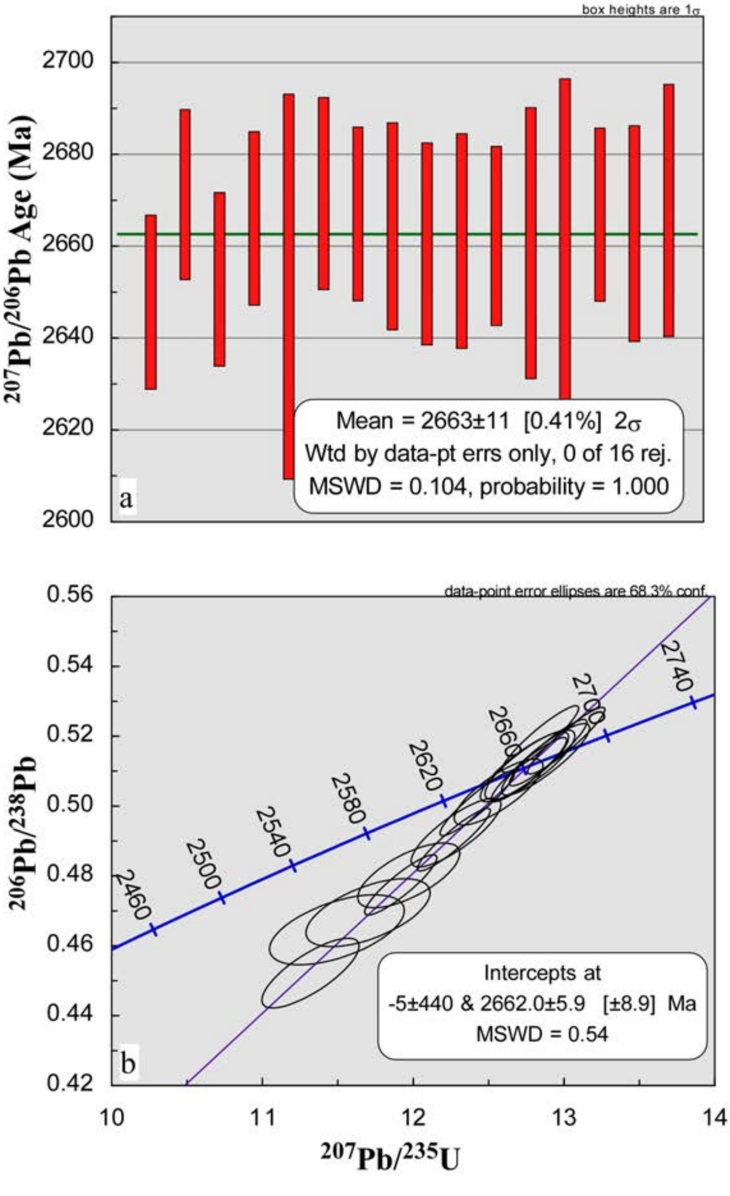
box heights are 1σ
2700
2680
2660
2640
2620
2600
207Pb/206Pb Age (Ma)
Mean = 2663±11 [0.41%] 2σ
Wtd by data-pt errs only, 0 of 16 rej.
MSWD = 0.104, probability = 1.000
a
data-point error ellipses are 68.3% conf.
0.56
0.54
0.52
0.50
0.48
0.46
0.44
0.42
206Pb/238Pb
2460
2500
2540
2580
2620
2660
2700
2740
Intercepts at
-5±440 & 2662.0±5.9 [±8.9] Ma
MSWD = 0.54
b
10
11
12
13
14
207Pb/235U

Figure 11

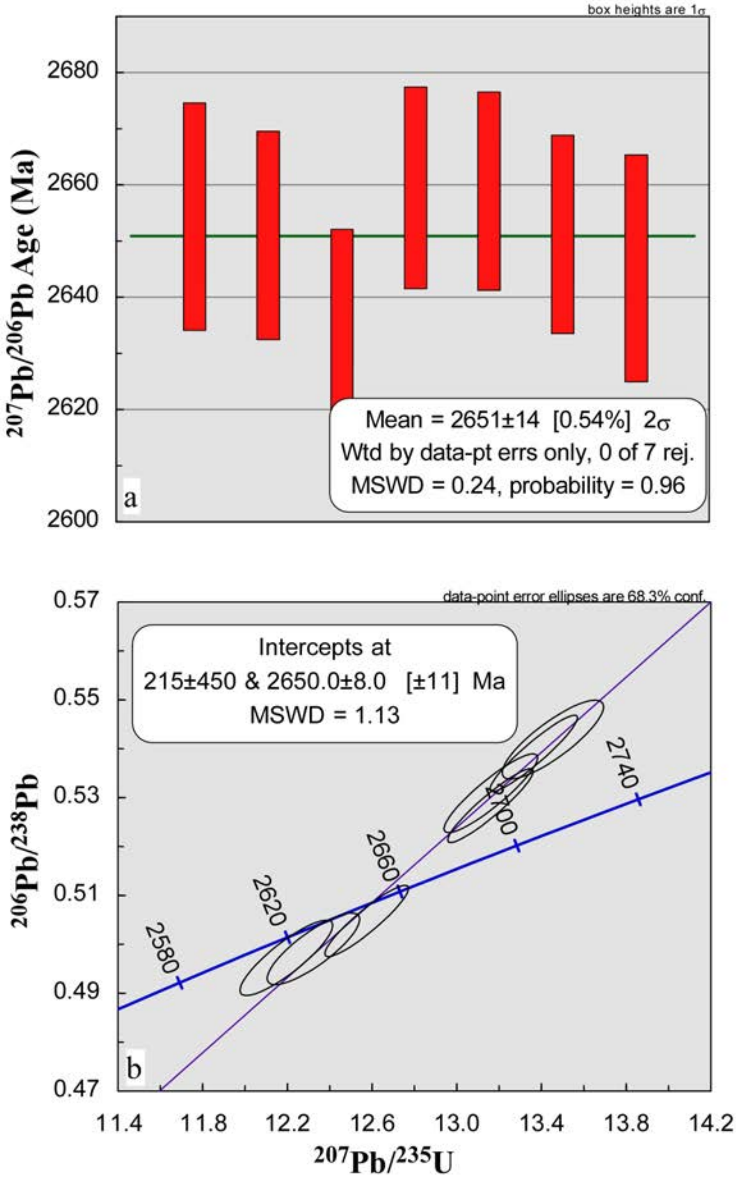
box heights are 1σ
2680
2660
2640
2620
2600
^{207}Pb/^{206}Pb Age (Ma)
Mean = 2651±14 [0.54%] 2σ
Wtd by data-pt errs only, 0 of 7 rej.
MSWD = 0.24, probability = 0.96
a
data-point error ellipses are 68.3% conf.
Intercepts at
215±450 & 2650.0±8.0 [±11] Ma
MSWD = 1.13
0.57
0.55
0.53
0.51
0.49
0.47
2740
2700
2660
2620
2580
^{206}Pb/^{238}Pb
b
11.4
11.8
12.2
12.6
13.0
13.4
13.8
14.2
^{207}Pb/^{235}U

Figure 12

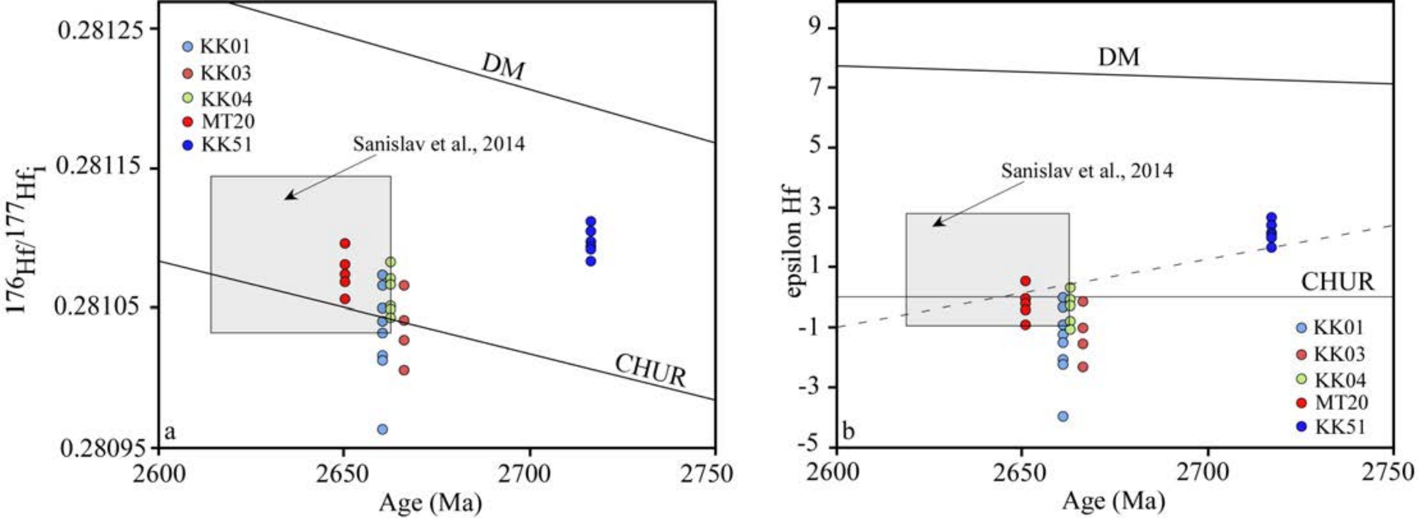

0.28125
0.28115
0.28105
0.28095
$^{176}Hf/^{177}Hf_i$
KK01
KK03
KK04
MT20
KK51
DM
CHUR
Sanislav et al., 2014
a
2600
2650
2700
2750
Age (Ma)
9
7
5
3
1
-1
-3
-5
epsilon Hf
DM
CHUR
Sanislav et al., 2014
KK01
KK03
KK04
MT20
KK51
b
2600
2650
2700
2750
Age (Ma)

Figure 13

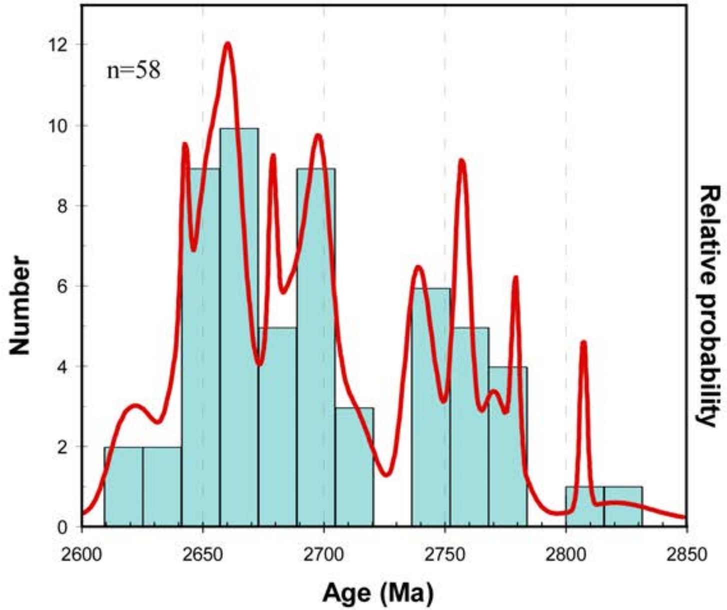

n=58
Number
Relative probability
Age (Ma)
0
2
4
6
8
10
12
2600
2650
2700
2750
2800
2850

Figure 14